OBJECT DETECTION WITH SECTOR SCANNING SONAR

Chew Jee Loong

BEng(Hons), University of Western Australia

A THESIS SUBMITTED
FOR THE DEGREE OF MASTER OF ENGINEERING
DEPARTMENT OF ELECTRICAL AND COMPUTER
ENGINEERING
NATIONAL UNIVERSITY OF SINGAPORE
2013

Declaration

I hereby declare that this thesis is my original work and it has been written by me in its entirety. I have duly acknowledged all the sources of information which have been used in the thesis.

This thesis has also not been submitted for any degree in any university previously.

Chew Jee Loong

14^{th} Nov, 2013

Acknowledgements

I would like to express my appreciations to my family and loved ones that have supported me throughout this passion of mine. I also wish to acknowledge the guidance and advice provided by Dr Mandar Chitre for his valuable and constructive inputs throughout the planning and development of this research work. My grateful thanks are also extended to the staff and students at Acoustic Research Lab and Tropical Marine Science Institute for their help and support in many various trials and work.

Contents

Summary

An object detection subsystem serves to detect obstacles that are in the vicinity of an Autonomous Underwater Vehicle (AUV). Along with the obstacle avoidance, command and control subsystems, it ensures that the AUV can safely execute and complete its mission. The first challenge is identifying a detection system. The sector scanning sonar was considered over other acoustic alternatives such as echosounders and multibeam as a means for object detection for STARFISH AUVs. The reasons are because of its compact size, lower power consumption and lower data rates. Upon successful hardware and software integration of the sector scanning sonar with the AUV, the next challenge is to develop a reliable object detection subsystem.

Experiments were planned to analyze the scanline measurements from the sector scanning sonar. In addition, the datasets were used to analyze the results of the detection and representation methodologies. Several operating environments with both static and dynamic setups are considered. Two experiments were conducted where the sector scanning sonar was deployed statically at Nanyang Technological University (NTU)'s diving pool and Republic of Singapore Yacht Club (RSYC). In both of these experiments, datasets were collected from the ensonification of static objects using the Micron DST sector scanning sonar. An experiment with STARFISH AUV integrated with Micron DST sector scanning sonar was also conducted at Pandan Reservoir. In this experiment, dataset was collected from the ensonification of the embankments and static buoys. Another experimental dataset was made available online by University of Girona at the Fluvia Nautic abandoned marina near St Pere Pescador (Spain) on 16 March 2007. In this setup, a Tritech Miniking sector scanning sonar attached to a moving Autonomous Underwater Vehicle (AUV) was deployed to ensonify the marina. The objects detected here were mainly the marina's embankments.

The scanline measurements from the sector scanning sonar were analyzed to understand how each element in the scanline measurement corresponds to the intensity return for a given bearing and range bin i. Then, detection and representation methods were explored to determine suitable approaches to represent both the operating environment and detection decisions made from the sonar measurements. The detection methodologies that were considered are Otsu thresholding and static thresholding. The formulation of the static thresholding was based on an adaptive threshold methodology with constant false alarm rate (CFAR). A mean statistic of the binary detections was used to represent the result from the Otsu threshold. Occupancy grid was used together with the static threshold to represent the probabilistic result of object detection.

Both Otsu thresholding and static thresholding are employed for the four experimental datasets. The Otsu threshold works well for the NTU, RSYC and Girona datasets but failed drastically for the Pandan Reservoir dataset. The static threshold works well across all the four experimental datasets. The static threshold is more effective as the assignment of the probability of a target given the sonar measurement is based on the decision statistic. Thus, measurement that marginally exceeds the threshold does not yield high probability of an object. The probabilistic detection decision was incorporated into the occupancy grid to attain the probability of occupancy. The probability of occupancy for each grid cells can be independently updated as and when more measurements are attained. The occupancy grid also proves to be an effective representation of the environment. The occupancy grid was also effective in localizing the AUV along with the objects.

List of Tables

List of Figures

Abbreviations

AUV	Autonomous Underwater Vehicle
CFAR	Constant False Alarm Rate
NTU	Nanyang Technological University
ROC	Receiver Operating Characteristic
RSYC	Republic of Singapore Yacht Club
SMB	Surface Marker Buoy
SNR	Signal to Noise Ratio
STARFISH	Small Team of Autonomous Robotic "Fish"

Physical Constants

Speed of Sound in Seawater	c	$=$	$1540\ \mathrm{ms}^{-1}$

Symbols

$s(\theta, i)$	Measurement for a given bearing θ and range bin i
$s_B(i)$	Background measurement at range bin i
$\tilde{S}$	Decision statistic
Z	Threshold
n_j	Number of measurements at the j-th level of the dynamic range
L	Maximum dynamic range of the sonar which is 255
C_0	Background class
C_1	Foreground class
w_0	Probability of occurrence for C_0

w_1	Probability of occurrence for C_1
u_0	Mean level for class C_0
u_1	Mean level for class C_1
σ_B^2	Between class variance
X_i	Background statistics for adaptive threshold at range bin i
K	Threshold constant for adaptive threshold
N_i	Number of background measurements at range bin i
P_D	Probability of Detection
P_{FA}	Probability of False Alarm
$\bar{X}$	Signal to noise ratio
P_T	Probability of a target given a single measurement
P_O	Probability of an object present
$l_{x,y}^{(t)}$	Log-odds ratio of $P(m_{x,y}\|s_{x,y}^{(1:t)})$

$l_{x,y}^{(0)}$	Initialization of log-odds ratio of probability of occupancy against the probability of non-occupancy
$l_{x,y}^{(t-1)}$	Log-odds ratio of the prior timestep $t-1$
$m_{x,y}$	Occupancy grid cell at position x, y
$s_{x,y}^{(t)}$	Measurement of position x, y at timestep t
$s_{x,y}^{(1:t)}$	Measurements of position x, y from timestep 1 to t
$P(m_{x,y})$	Probability of occupancy for position x, y
$P(m_{x,y}\|s_{x,y}^{(t)})$	Probability of occupancy given the current measurement for position x, y
$P(m_{x,y}\|s_{x,y}^{(1:t)})$	Probability of occupancy for position x, y conditional on the measurements from timestep 1 to t

Chapter 1

Introduction

The object detection subsystem plays a crucial role in supporting the operations of an AUV and it is the foundation that leads to an obstacle avoidance subsystem. Along with the command and control (C2) subsystem, it ensures the safety of the vehicle by detecting objects in the vicinity of the AUV.

1.1 Background and Motivation

The STARFISH AUVs [1, 2] are a team of modular and low-cost autonomous underwater vehicles (AUVs) with a design that supports extensions to add heterogeneous capabilities. An open-architecture framework that includes mechanical, electrical and software interfaces was incorporated into the design of STARFISH AUVs. This allows users to easily integrate their proprietary modules with the AUV and also permits the insertion and swapping of software subsystems within the vehicle to alter any desired aspect of the vehicle. In Fig. 1.1, we have a view of 2 STARFISH AUVs called Redstar and Bluestar during one of the open water trials at Selat Pauh, Singapore.

FIGURE 1.1: Redstar & Bluestar

An object detection subsystem serves to detect obstacles that are in the vicinity of the AUV. Along with the obstacle avoidance, command and control subsystems, it ensures that the AUV can safely execute and complete its mission. There are many challenges with the implementation of an object detection subsystem for an AUV. The first challenge is in identification of a detection system. Typically for an AUV, object detection can be achieved through acoustic and/or video imaging means. Acoustic sensing is more suitable for in-water operations as compared to video imaging sensing. This is primarily because sound waves travel further in water, and thus it allows for further sensing range.

There are various types of acoustic sensors such as echosounder, sector scanning sonar, multibeam sonar and forward looking bathymetry sonar. Current approaches mainly rely on the implementation of a multibeam sonar as it is able to yield readily interpretable images. In the STARFISH AUVs [1, 2], the considerations for implementing the sector scanning sonar over a multibeam sonar are:

Data	The data output for a sector scanning sonar for each bearing ensonification is an array, with its array size dependent on a configured range or resolution. A multibeam sonar typically yields readily interpretable images but at much higher data rate.
Size	The sector scanning sonar is more compact in terms of mechanical dimensions and integrates comfortably in the nose module of the STARFISH AUV.
Power	The sector scanning sonar consumes less operating power.

The next challenge is to develop a reliable object detection subsystem. The object detection subsystem typically consists of detection and representation methodologies. The detection methodology is responsible to process and analyze the sonar data to determine whether an object is present or absent. The representation methodology is firstly used to localize the position of the AUV. Secondly, it is used to map and represent the environment. The motivation is to determine suitable detection and representation methodologies that can be employed for an AUV using a sector scanning sonar.

An AUV can be deployed in various types of operating environments from a confined water facilities to an open water environment. Thus, another motivation is to achieve an effective and reliable object detection using a sector scanning sonar across as many operating environments as possible.

1.2 Contributions

- We propose annular statistics instead of radial statistics and implement the computation of background statistics based on annular statistics. We introduce the decision statistic which represents the difference between a measurement and its respective background estimate.

- We adopt the formulation of a threshold based on an adaptive thresholding methodology with constant false alarm rate (CFAR). We compute the probability of a target as a function of the decision statistic. We are then able to make probabilistic statement of object detection.

- We adopt the formulation of occupancy grid as a representation methodology. We use the occupancy grid to map and represent the environment along with the localization of the AUV and objects.

- We incorporate the probabilistic detection decision from the static threshold into the occupancy grid to develop an object detection subsystem.

- We analyze the results of object detection using a sector scanning sonar from several experimental datasets at different operating environments for both static and dynamic setups. We also benchmark the results using static thresholding against Otsu thresholding and median statistics.

1.3 Literature Review

The simplest sonar detection problem is to decide from the return of a sonar ping whether an object is present or not. In a sonar measurement, the representation of an object is ideally a signal reading with an amplitude higher than the background. However, the sonar measurement is also riddled with noise from various sources (i.e. thermal noise, electrical noise, acoustic noise and multipath reverberations).

The ability for any sonar to decide whether an object has been detected or not begins with detection theory. It is in detection theory where binary and/or probabilistic statements can be made about whether objects are detected or not. The simplest approach to discriminate an object from its background is using static thresholding. If the signal's amplitude from the sonar measurement exceeds the threshold value, it would be an indication of an object. If the threshold is set to a low value, the thresholding method potentially yields high false alarm. On the other hand, if it is set to a high value, valid objects are easily missed. These are the drawbacks to static thresholding.

A variant of static thresholding is the Otsu thresholding [3]. The thresholding method is based on the zeroth-and the first-order cumulative moments of the gray-level histogram. The numbers of gray-level can be mapped to the dynamic range of the sonar measurements. Assuming a bimodal histogram, this method attempts to determine a threshold, Z, that can be used to discriminate the 2 modes; with one of the mode representing the background data while the other mode is of the foreground or object(s). In [4], the authors indirectly implemented an algorithm similar to Otsu thresholding. The authors first create a smoothed histogram of the data and attempt to determine the modes of the distribution. Depending on the number of modes and their potential representation of low and high echo return strength, a threshold value between the modes will be used for static thresholding.

A double or 2-level thresholding can be employed to extend the concept of static thresholding. Measurement above the high threshold and below the low threshold are classified respectively as an object and background. Measurement between the low and high thresholds can be classified as object only if there adjacent measurement that are classified as object. In [5], the author implemented a 2-level thresholding on the measurement data for object detection. However, it suffers similar drawbacks of static thresholding where there are potentially false alarms and missed targets. The other approach is adaptive/dynamic thresholding [6, 7]. In addition, the concept of constant false alarm rates (CFAR) [6] was introduced. The objective of the adaptive thresholding is to attain a constant false alarm rate despite varying interference power levels. In [6], the authors proposed an adaptive threshold estimated based on the standard deviation of a background data along with along a scaling constant. The scaling constant was estimated based on a desired probability of false alarm.

Several other CFAR variants such as Cell Averaging CFAR (CA-CFAR), Smallest Of CFAR (SO-CFAR), Greatest Of CFAR (GO-CFAR) and Variable Index CFAR (VI-CFAR) [8, 9, 10, 11] can be easily found. However, most of the literature and applications of CFAR are inclined towards radar processing rather than sonar processing. Radar easily has range detection from 10km to 100km while the sector scanning sonar used on the STARFISH AUVs [1, 2] only has a maximum range of 75m. Radar then has the opportunity for more measurements while approaching a target. CFAR algorithms easily rely on more than 100 measurements for a good approximation of background statistics. We can increase the resolution of the sonar measurement to increase the number of measurements. However, resolution of less than 1m would not provide any other advantages in the interest of object detection and avoidance.

In [12], the authors firstly filtered the measurement data using a sliding window algorithm, which is an algorithm similar to the CA-CFAR. This was followed with a Otsu gray-level thresholding on an image sequence. In a subsequent paper, [13] firstly filtered the measurement data using a 1-level intensity thresholding based on the mean and standard deviation of the measurement data. Then, a fuzzy detector was applied on the pre-processed measurement data for object detection. Image processing was further applied on frame sequences. Image processing techniques for object detection have been observed on several sonar-related literature [14, 12, 13]. Image processing techniques are employed on a sequential set of scanline measurements collated as an image. These techniques are computationally expensive in terms of processing time and memory allocation. On top of that, the collation of a sequential set of sonar pings decreases the real-timeness of the object detection process.

In addition to the object detection subsystem, there should be means to map and represent the operating environment. In [15], the author introduced occupancy grid to represent a map of the environment in an evenly spaced cell manner. Based on the location of the AUV, bearing and range of sonar ensonification, the measurements are mapped to the respective x-y positioning of the occupancy grid. In each cell, information pertaining to occupancy is stored. Whenever a cell is ensonified by the sonar, its probability of occupancy is updated based on the cell's object detection methodology.

1.4 Thesis Layout

Chapter 2 introduces the tools and methodology employed for the development of an object detection system. In the first section, the Tritech Micron DST sector scanning sonar [16] along with the acquisition mechanics of the scanline measurement will be introduced. The subsequent sections will be on detection and representation methodologies that can be employed.

The Otsu threshold [3] and static thresholding based on an adaptive thresholding methodology with constant false alarm rate (CFAR) [6] will be introduced as possible detection methods. The representation methodology will outline how the occupancy grid can be used to represent the operating environment of the AUV along with its relations to the sonar measurement. The probabilistic formulation of its grid cells to store the probability of occupancy will also be presented.

Chapter 3 and Chapter 4 present a static experimental dataset collected respectively at Nanyang Technological University (NTU) and Republic of Singapore Yacht Club (RSYC). In this setup, a stationary sector scanning sonar was deployed to ensonified potential static targets both at NTU and RSYC.

Chapter 5 presents an experimental dataset collected with the sector scanning sonar integrated on STARFISH AUV at Pandan Reservoir. In this setup, the sector scanning sonar was ensonifying the embankments and static buoys. Chapter 6 explores the experimental dataset collected by University of Girona [17]. The Girona dataset consists of a dynamically moving AUV scanning the marina's embankment.

We discuss the findings and results comparing the implementation using the Otsu threshold and the adaptive threshold for the experimental datasets. There are also discussion on the background statistics, measurement statistics, probability of a target given a single measurement, probability of occupancy given the current measurement, occupancy grid and the effectiveness of the respective threshold. Lastly, conclusion and potential future works are discussed in Chapter 7.

1.5 List of Publication

1. J. L. Chew and M. Chitre, "Object detection with sector scanning sonar," in *OCEANS 2013 IEEE - San Diego*, Sept 2013.

Chapter 2

Tools and Methodology

2.1 Sector Scanning Sonar

We introduce the Micron DST sector scanning sonar [16] that is integrated on STARFISH AUVs [1, 2]. The understanding of the scanline measurement along with information pertaining to annular statistics, decision statistic and Receiver Operating Characteristic (ROC) are presented.

2.1.1 Micron DST

We are using the Micron DST sector scanning sonar by Tritech International on STARFISH AUVs. The experiments at NTU, RSYC and Pandan Reservoir were also conducted using the Micron DST sector scanning sonar.

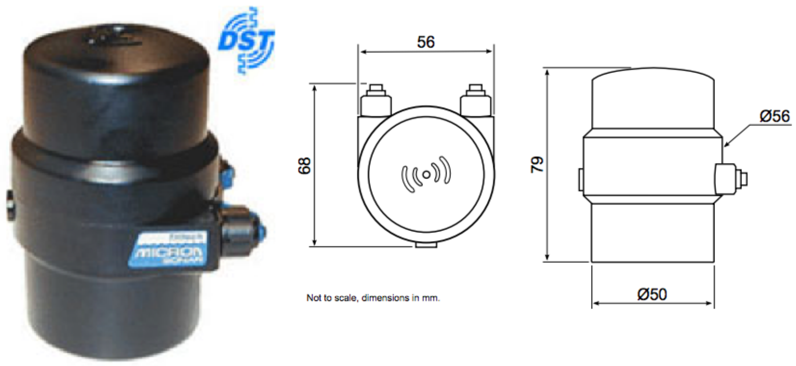

FIGURE 2.1: Micron DST sector scanning sonar

It is more compact in terms of mechanical dimensions and requires less operating power as compared to other sonars such as the multibeam and forward looking bathymetry sonars. The specifications of the Micron DST sector scanning sonar is as follows:

Frequency	Chirping between 650kHz to 750kHz
Vertical beamwidth	35°
Horizontal beamwidth	3°
Range	Settings from 2m (6 ft) to 75m (250 ft)
Power requirements	12V DC 50V @ 4VA (Average)
Data communication	RS 232 (via modem up to 115kb/s)
Weight in air	324 g
Weight in water	180 g

TABLE 2.1: Specifications of the Micron DST sector scanning sonar

2.1.2 Scanline Measurement

A sector scanning sonar ensonifies a sector of an area where the sonar is directed at for a given bearing, range and resolution. The range and resolution of the sector scanning sonar is usually represented by the number of range bins. Thus, each element in the scanline measurement, $s(\theta, i)$, corresponds to the intensity return for a given bearing θ and range bin i. Based on the location of the AUV, bearing and range of sonar ensonification, we can determine the respective x-y positioning of the occupancy grid cell and update it with the latest measurement. This approach is easily implementable for a static setup and is also extensible to a dynamic setup where the sonar is mounted on a moving platform or vehicle.

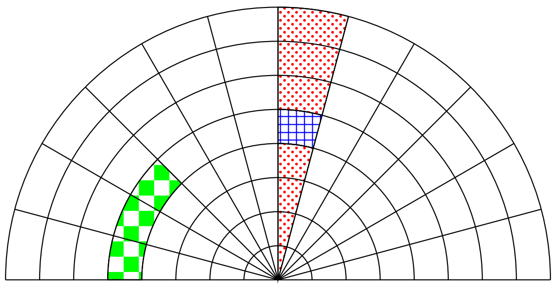

FIGURE 2.2: Methodology to determine annular statistics

Fig. 2.2 depicts a sector of grid cells for a statically deployed sector scanning sonar. The Micron DST sector scanning sonar is mechanically steered. Thus, scanline measurements are progressively acquired according to bearing. The desired cell along with its neighbouring cells depicted respectively as blue-colored grid cell and red-colored crosshatch dots cells in

Fig. 2.2 form the scanline measurements acquired for a particular bearing. Even though the scanline measurements are acquired with regards to a particular bearing, the annular statistics according to range or bin are of more statistical importance. This is primarily because the ensonification of an area at a particular range or bin typically are of similar statistics. The scanline measurements for a similar range or bin would suffer from the same 2-way propagation loss and similar processing gain would be applied. The blue-colored grid cell and the green-colored checkerboard cells in Fig. 2.2 form the annular statistics for a particular range bin. The green-colored checkerboard cells have been depicted to only extend across several bearings to maintain clarity to the figure. The green-colored checkerboard cells should extend across the bearings where the background sector is identified. The annular statistics should be computed for a background sector free of any objects. Otherwise, the background estimate for the computation of the decision statistic in Section 2.1.3 might be higher.

2.1.3 Decision Statistic

The decision statistic $\tilde{S}$ is the difference between measurement $s(\theta, i)$ and its respective background estimate $s_B(i)$ at range bin i. It is defined as follows:

$$\tilde{S} = s(\theta, i) - s_B(i) \tag{2.1}$$

The decision statistic $\tilde{S}$ is affected by the choice of dynamic range. The Micron DST sonar can be configured for either a 4-bit or 8-bit dynamic range that respectively yields measurements between 0 to 15 and 0 to 255. We consider the 8-bit dynamic range as it provides more measurement resolution. In addition, the 8-bit dynamic range potentially allows for a higher $\tilde{S}$. The sonar measurements are logarithmic with the intensity return where the lowest and highest measurement for either the 4-bit or 8-bit dynamic range still map to 0 dB and 80 dB. Thus, the decision statistic is effectively a ratio and therefore it is scale invariant.

The decision statistic $\tilde{S}$ is used to determine P_T which is the probability of a target given a single measurement. P_T will be presented in Section 2.2.2. If we consider annular statistics as in Fig. 2.2, the measurement $s(\theta, i)$ would be the blue-colored grid cell while the respective background estimate $s_B(i)$ could be the mean or median of the green-colored checkerboard cells. In this thesis, we consider the background estimate $s_B(i)$ to be the median of the annular background statistics.

2.1.4 Receiver Operating Characteristic

Receiver Operating Characteristic (ROC) or simply ROC curve is a graphical plot that is used to assess the performance of a sonar detector for an object. It is a plot of probability of detection, P_D, against the probability of false alarm, P_{FA}. A perfect detector will have an ideal ROC curve that start at the origin (0,0), go vertically up the y-axis to (0,1) and then horizontally across to (1,1). This means that we can attain unity P_D for a zero P_{FA}. A good detector would be somewhere close to this ideal.

Firstly, we collect the measurements of an object at range bin i. We then sequentially vary a threshold value from the lowest possible measurement value to its maximum possible value and note the number of measurements of the valid object that exceeds the threshold. The P_D at each threshold value is computed as the number of measurements that exceeds the threshold value divided by the number of measurements of the valid object. The computation of P_{FA} is similar to the computation for the P_D. However, the measurements are from a non-object at similar range bin i. Finally, we plot P_D against P_{FA} to obtain the ROC curve.

2.2 Detection Methodology

There are various methodologies that can be employed to decide whether an object is present or otherwise. The idea is to be able to discriminate the measurement against an estimated background noise. Examples with increasing complexity include single/static thresholding, double thresholding and adaptive thresholding. If single or double thresholding is considered, the difficulty lies with determining a threshold that adapts to the environment in accordance with a false alarm rate. An optimum threshold [8, 10] can be achieved if only one is certain of the background noise. An example of a single thresholding methodology that adapts to the environment is the Otsu thresholding. However, Otsu thresholding is an image processing methodology. In the implementation of an adaptive threshold, the background noise is typically estimated based on the neighbouring cells of the measurement. On top of that, a scaling constant imbued with constant false alarm is also incorporated.

2.2.1 Otsu Threshold

We introduce the Otsu thresholding [3] that attempts to determine a threshold that discriminates the background and foreground modes. If a measurement exceeds the threshold, a binary decision can be made stating that an object is detected. Firstly, the measurements are represented in $(L + 1)$ levels. The number of measurements at each of the histogram bin, j, is denoted by n_j. Next, the probability distribution of the measurements are determined from the normalized histogram as follows:

$$p_j = \frac{n_j}{\sum\limits_{j=0}^{L} n_j} \tag{2.2}$$

where

n_j	is the number of measurements at the j-th level of the dynamic range
L	is the maximum level of the dynamic range for the sonar which is 255

Assuming that there is a threshold Z, the threshold divides the measurements into background and foreground classes namely, C_0 and C_1. Thus, C_0 accounts for the measurements ranging from 0 to Z, while C_1 accounts for measurements ranging from $(Z+1)$ to L. Then, the probabilities of class occurrence can be determined as follows:

$$w_0 = \sum_{j=0}^{Z} p_j \tag{2.3}$$

$$w_1 = 1 - \sum_{j=0}^{Z} p_j \tag{2.4}$$

The class mean levels can is determined as follows:

$$u_0 = \sum_{j=0}^{Z} \frac{(j+1)p_j}{w_0} \tag{2.5}$$

$$u_1 = \sum_{j=Z+1}^{L} \frac{(j+1)p_j}{w_1} \tag{2.6}$$

where

w_0	is the probability of occurrence for C_0. It is also known as the zeroth-order cumulative moment of the histogram up to the Z-th level
w_1	is the probability of occurrence for C_1
u_0	is the mean level for class C_0
u_1	is the mean level for class C_1

The between-class variance is determined as follows:

$$\sigma_B^2 = w_0 w_1 (u_1 - u_0)^2 \tag{2.7}$$

Finally, the optimal threshold Z^* is determined where the selected threshold value would maximize the between-class variance.

$$Z^* = \underset{0 \leq Z < L}{\arg\max}\, \sigma_B^2(Z) \tag{2.8}$$

This thresholding method is typically used with an image processing methodology where all the pixels of the given image are evaluated as a whole. The data from a sector scanning sonar is only a scanline measurement which is basically an array of measurements. Thus, we will need to collate several adjacent and continuous scanline measurements to form a sectorial image before we apply the Otsu thresholding methodology.

2.2.2 Static Threshold

We introduce a threshold based on an adaptive threshold [6] methodology incorporating a constant false alarm rate (CFAR). Firstly, we introduce the formulation of the adaptive threshold. The adaptive threshold Z for range bin i is constructed based on the estimate of the background statistics, X_i, along with the number of background measurements, N_i, and a threshold constant, K. If we were to consider the neighbouring bins as the background statistics, it is assumed that the first order probability density function of the background statistics X_i to be Rayleigh distributed. The formulation of the adaptive threshold Z is as follows [6]:

$$Z = K\sqrt{\frac{1}{N_i}\sum_{i=1}^{N_i} X_i^2} \tag{2.9}$$

The threshold constant K can be computed based on a desired probability of false alarm, P_{FA} as follows [6]:

$$K = \sqrt{\left[(P_{FA})^{-\frac{1}{N_i}} - 1\right] N_i} \tag{2.10}$$

Assuming a Swerling III object model [18, 6], the probability of detection, P_D can be determined as follows [6]:

$$P_D = \left(\frac{\bar{X}+2}{\bar{X}+2+\frac{2K^2}{N_i}} \right)^{N_i} \left[1 + \left[\frac{2K^2\bar{X}}{(\bar{X}+2)(\bar{X}+2+\frac{2K}{N_i})} \right] \right] \tag{2.11}$$

where

$\bar{X}$ is the average signal to noise ratio (SNR)

In [6], the authors considered the background statistics, X_i, to be from neighbouring bins of the desired target bin and they are of similar heading or bearing. This is illustrated with the desired bin being the blue-colored grid cell while the neighbouring bins are the red-colored crosshatch dots cells as depicted in Fig. 2.2. In this thesis, we consider annular statistics where the desired target are compared with background statistics that are of similar range bin. This is illustrated with the desired bin being the blue-colored grid cell while the background bins are the green-colored checkerboard cells as depicted in Fig. 2.2. We assume that the background statistics X_i for our datasets to be Rayleigh distributed. Besides that, we consider the median of the annular background statistics as the estimate of the background noise. A higher number of background measurements, N_i, improve the estimate of the background noise. This leads to an increase of the probability of detection, P_D. Based on the approach of annular statistics, the size and the number of ensonifications of the background sector determine N_i. Thus, we can consider more ensonifications and a larger background sector to improve the estimate of the background noise and probability of detection. We use the background noise estimate to normalize our decision statistic $\tilde{S}$ in (2.1).

We will not solely rely on the adaptive threshold Z to determine a binary decision whether an object is indeed detected or not. We instead compute P_T which is the probability of a target given a measurement and incorporate it into the formulation of occupancy grid which will be presented in Section 2.3. This allows us to make probabilistic statement of object detection. We adopt the detection probability P_D and $\bar{X}$ in (2.11) respectively as P_T and the decision statistic $\tilde{S}$. This is because P_D and P_T have similar formulation based on background statistics. In addition, we also assume a Swerling III object model and Rayleigh distribution for the background statistics. The advantage is that we will be able to compute the P_T of any target as a function of its detection statistic $\tilde{S}$. P_T is defined as follows:

$$P_T = \left(\frac{\tilde{S}+2}{\tilde{S}+2+\frac{2K^2}{N_i}} \right)^{N_i} \left[1 + \left[\frac{2K^2\tilde{S}}{(\tilde{S}+2)(\tilde{S}+2+\frac{2K}{N_i})} \right] \right] \tag{2.12}$$

P_T is a function of the detection statistic $\tilde{S}$. The larger $\tilde{S}$ is, the higher P_T will be. As a larger dynamic range does not necessarily yield higher $\tilde{S}$ as explained in Section 2.1.3, P_T might not be necessarily higher by merely increasing the dynamic range. In addition, the possible value for P_T is between 0 and 1 if we consider the 8-bit dynamic range.

The background sector can be identified during the preparatory stage before the AUV executes the actual mission. Once we identify a background sector and are certain of the desired P_{FA}, the threshold constant K in (2.10) can be pre-computed before the actual mission. P_T in (2.12) can also be pre-computed as a look-up table because we know that the possible values for the decision statistic $\tilde{S}$ can only range from 0 to 255. The advantage is that there is no need to store the measurement as the analysis of the static thresholding can be made as soon as the measurement is acquired.

2.3 Occupancy Grid

An AUV subsystem for obstacle detection should include a means to map and represent the operating environment of the AUV. This can for example be done using occupancy grids [15] which represent the environment in an evenly spaced cell manner. The representation of the environment with grid cells is rather similar to how the elements in the scanline measurement represent spatial information. In each cell, information pertaining to occupancy is stored. Whenever a cell is ensonified by the sonar, the potential of occupancy of the respective ensonified cells can be updated based on the cell's object detection methodology.

We use the occupancy grid as a representation methodology for both Otsu thresholding and static thresholding. However, the occupancy grid for Otsu thresholding is of binary representation while it is of probabilistic representation for static thresholding. There are many formulations for the probability of occupancy. In this thesis, we adopt the formulation of the log-odds ratio described in [19]. It is as follows:

$$\begin{aligned} l_{x,y}^{(t)} &= \log \frac{P(m_{x,y}|s_{x,y}^{(1:t)})}{1 - P(m_{x,y}|s_{x,y}^{(1:t)})} \\ &= \log \frac{P(m_{x,y}|s_{x,y}^{(t)})}{1 - P(m_{x,y}|s_{x,y}^{(t)})} + \log \frac{1 - P(m_{x,y})}{P(m_{x,y})} + l_{x,y}^{(t-1)} \end{aligned} \tag{2.13}$$

where

$l_{x,y}^{(t)}$	is the log-odds ratio of $P(m_{x,y}\|s_{x,y}^{(1:t)})$ at timestep t
$s_{x,y}^{(t)}$	is the measurement of position x, y at timestep t
$s_{x,y}^{(1:t)}$	is the measurements of position x, y from timestep 1 to t
$m_{x,y}$	is the occupancy grid cell at position x, y
$P(m_{x,y})$	is the probability of occupancy for position x, y
$P(m_{x,y}\|s_{x,y}^{(t)})$	is the probability of occupancy given the current measurement for position x, y
$P(m_{x,y}\|s_{x,y}^{(1:t)})$	is the probability of occupancy for position x, y conditional on the measurements from timestep 1 to t
P_O	is the probability of an object present and we introduce it as a simpler abbreviation for $P(m_{x,y}\|s_{x,y}^{(1:t)})$ as in (2.14)
$l_{x,y}^{(t-1)}$	is the log-odds ratio of the prior timestep $t-1$

$$P_O \equiv P(m_{x,y}|s_{x,y}^{(1:t)}) \tag{2.14}$$

The probability of occupancy $P(m_{x,y})$ is set to a value of 0.5. This is because we are unsure whether the grid cell is occupied or not. A value of 0.5 translates to a 50% chance of a grid cell being occupied. We adopt P_T in (2.12) as $P(m_{x,y}|s_{x,y}^{(t)})$ because both of them are probabilities of a target given a measurement. The initialization, $l_{x,y}^{(0)}$, is as follows:

$$l_{x,y}^{(0)} = \log \frac{P(m_{x,y})}{1 - P(m_{x,y})} \tag{2.15}$$

2.4 Summary

The Otsu thresholding will require the collation of several scanline measurements to form a sectorial image before the threshold can be determined. We then obtain the detection results of the measurements as a binary value. There are usually several iterations of Otsu thresholding as more sectorial image are obtained. The result of the occupancy grid for Otsu thresholding would be the mean of all the results.

We use the occupancy grid as a probabilistic representation methodology together with the static thresholding. The result of the occupancy grid for static thresholding would be the most recent computed value of P_O. The sequence of steps and information that we use to compute P_O are as follows:

1. Initialize the occupancy grid.

2. Determine a desired probability of false alarm, P_{FA}.
3. Identify a background sector during the calibration or preparatory stage of the mission.
4. Compute $s_B(i)$ which is the background estimate for range bin i. We compute the median of X_i which is the annular background statistics as explained in Section 2.1.3 and Fig. 2.2.
5. Compute threshold constant K in (2.10).
6. Attain a measurement $s(\theta, i)$.
7. Compute the decision statistic $\tilde{S}$ in (2.1).
8. Compute P_T which is the probability of a target given a measurement as in (2.12).
9. Adopt P_T as $P(m_{x,y}|s_{x,y}^{(t)})$ into occupancy grid as in (2.13).
10. Compute P_O which is probability of an object present as in (2.14).

Chapter 3

Experimental Data — Static Setup at NTU

3.1 Experimental Setup

An experiment with the Micron DST sonar was conducted at NTU's diving pool to investigate the capability of the sonar in discriminating static objects of different elevations. The diving pool provides a structured and controlled environment compared to typical environments where AUVs tend to be deployed. The advantages are that we can have a controlled placement of the objects and be certain of the dimension of the diving pool along with the exact location of the sonar. The objects placed in the diving pool are as follows:

Object A	An air tank placed at the pool bottom, with a surface marker buoy (SMB) hovering 2 meters from pool bottom.
Object B	An air tank placed at the pool bottom.
Object C	A buoy with a SMB hovering 3 meters from pool bottom, anchored with a base plate.

The dimension of the NTU's diving pool along with the experimental setup is depicted in Fig. 3.1 while an actual photograph of the experimental setup is in Fig. 3.2.

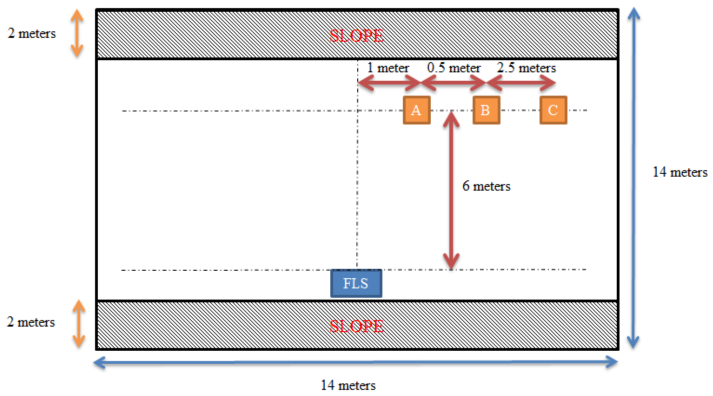

(a) Top view

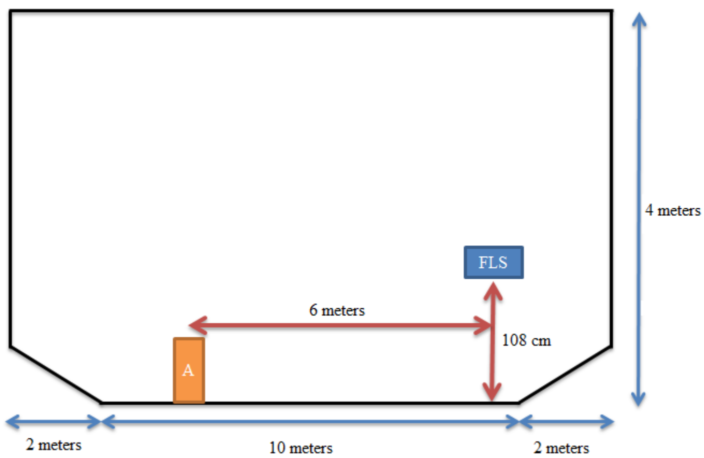

(b) Side view

FIGURE 3.1: Experimental setup at NTU's diving pool

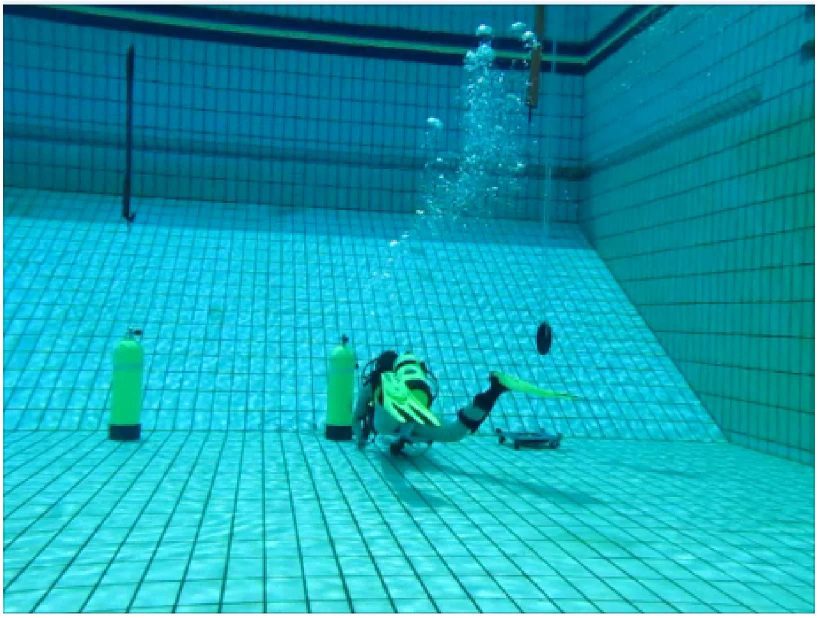

FIGURE 3.2: Photograph of the experimental setup at NTU's diving pool

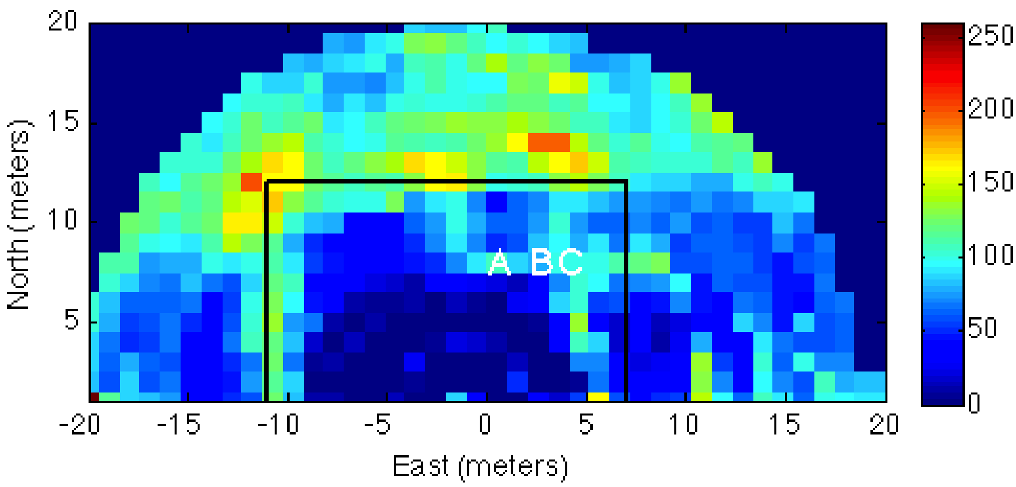

FIGURE 3.3: Median result of the measurements at NTU's diving pool

The boundary of the diving pool is depicted with black lines in Fig. 3.3. A ring of artifacts is observed in front of the sonar. The specular returns could be due to the reflections from the pool's bottom as the sonar was placed near the pool's bottom. There are also numerous artifacts detected outside the boundary of the walls. It is suspected that these are due to multipath reflections. The slope behind the objects is also detected. The portion of the frontal slope that is parallel to the sonar has the highest amplitude because the ping of the sonar is reflected directly back to the sonar. As for other portion of the slope, the ping of the sonar might be reflected at other directions. This is the reason for the decrease of amplitude at other portion of the slope.

3.2 Measurement Statistics

The measurements of the objects identified from the experiment are presented in Fig. 3.4 and Table 3.1.

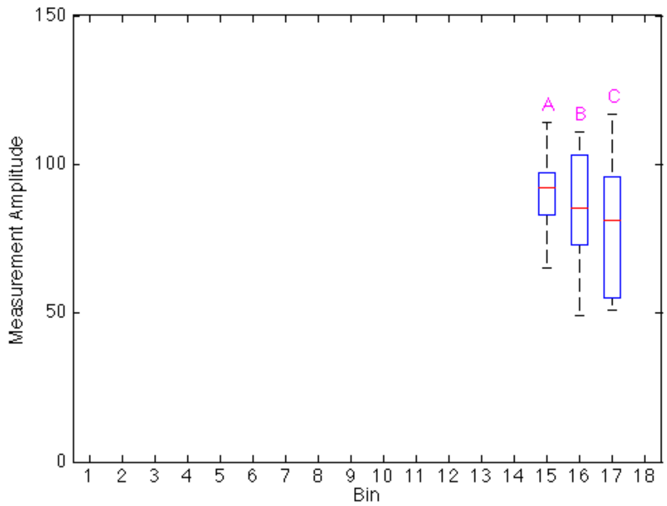

FIGURE 3.4: Measurements of the objects at NTU's diving pool

	Object		
	A	B	C
Distance (m)	7.6	8.2	8.7 m
Bearing (°)	113.5	127	94
Bin	15	16	17
Min	65	49	51
Median	92	85.5	81
Max	114	111	117

TABLE 3.1: Setup information and measurement statistics of the objects at NTU's diving pool

The measurements for all the objects are between 49 and 117. Object A has a median measurement that is slightly higher than the median measurement of object B. This is expected because object A has an additional SMB that is filled with air. Although object B and C are of different targets, the median measurement for object C is at 81 which is rather similar with object B. This could be because the disc is easily ensonified as it was elevated from the pool's bottom. Occasionally higher measurements were also observed for object C due to the increase of surface area ensonified as the disc rotates.

3.3 Receiver Operating Characteristic

Based on the measurements of the objects in Fig. 3.4, we can attain the ROC curves for the objects as presented from Fig. 3.5 to Fig. 3.7. All the objects have desirable ROC curves where high probability of detection can be achieved with rather low probability of false alarm.

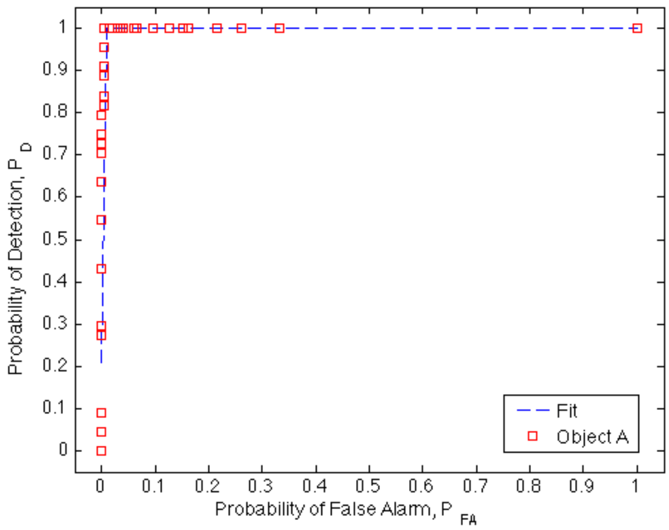

FIGURE 3.5: ROC of object A at NTU's diving pool[1]

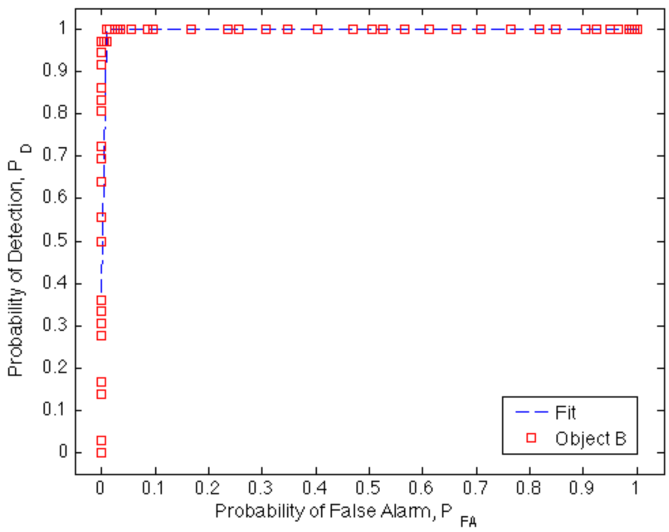

FIGURE 3.6: ROC of object B at NTU's diving pool[2]

[1]The fit used is $P_D = 1 + [-0.8031 \times \exp(-1605 \times P_{FA})]$.
[2]The fit used is $P_D = 1 + [-0.6324 \times \exp(-1259 \times P_{FA})]$.

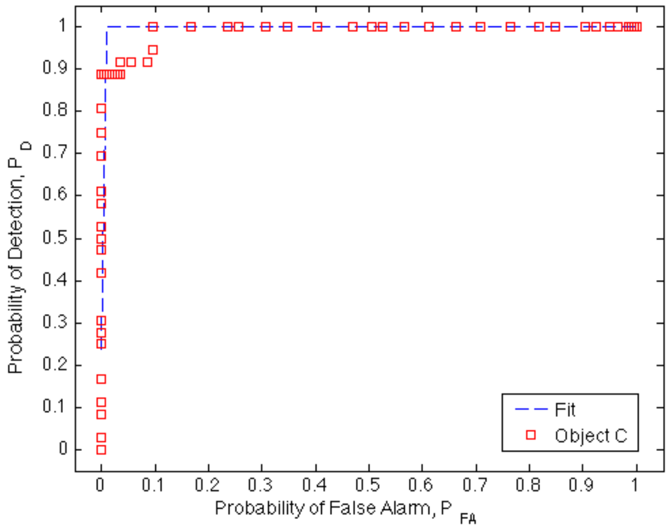

FIGURE 3.7: ROC of object C at NTU's diving pool[3]

3.4 Otsu Thresholding

The Otsu threshold in (2.8) is computed based on the statistics of several scanline measurements that were collated to form a sectorial image. We collated 30 scanline measurements to form the first sectorial image with a field of view of 90°. This is because the sector scanning sonar begins its ensonification looking ahead followed with a 90° rotation towards the starboard. Subsequently, we collated 60 scanline measurements to form a sectorial image with a field of view of 180° that spans all the way from starboard of the sonar till its portside. There were 9 iterations and the

[3]The fit used is $P_D = 1 + [-0.7759 \times \exp(-1234 \times P_{FA})]$.

thresholds determined are presented in Fig. 3.8. The median threshold determined is at the value of 62.

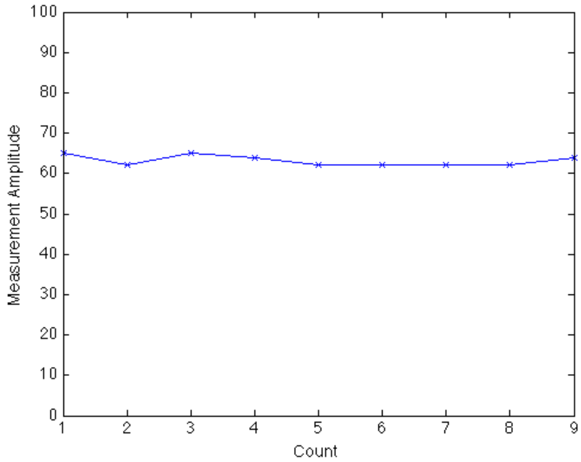

FIGURE 3.8: Otsu threshold for NTU dataset

3.4.1 Binary Occupancy Grid

The mean result of the binary occupancy grid is in Fig. 3.9. It is observed that the surrounding walls are easily detected with mean result close to 100% detection. The mean detection of the object A, B and C respectively are 100%, 94% and 68%. The portion of the frontal slope that is parallel to the sonar is easily detected with mean detection close to 100%. There is minimal detection for the slope towards the portside of the sonar although it has mean detection ranging from 0% to 100%. The slope towards the starboard has mean detection ranging from 20% to 100%. In addition, the artifacts between the sonar and the objects are filtered off by the thresholding. Artifacts are also observed beyond the boundary of the diving pool. The statistics of the binary detections are summarized in Table 3.2.

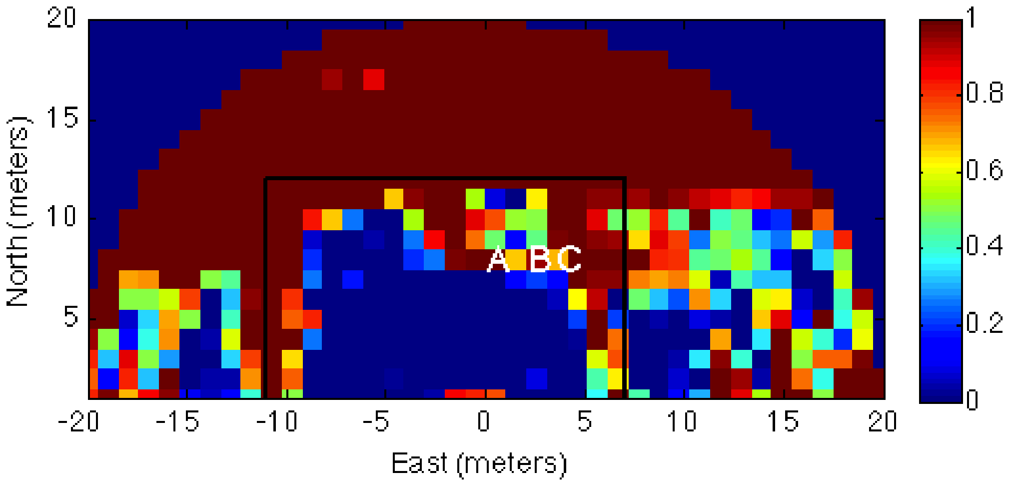

FIGURE 3.9: Mean result of the binary occupancy grid with Otsu thresholding for NTU dataset

In Fig. 3.10 to Fig. 3.12, we analyze the measurements of the objects against their respective Otsu threshold to understand the results of binary detection.

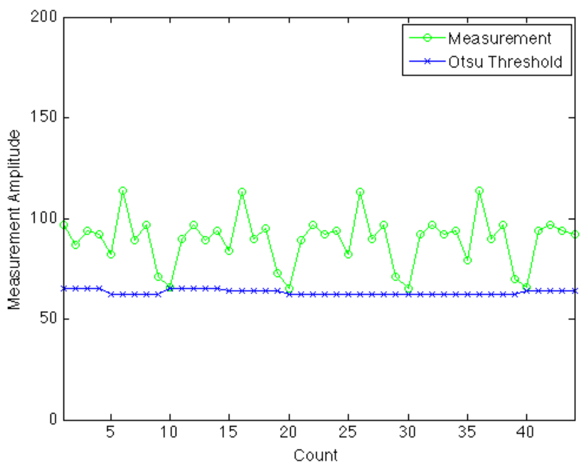

FIGURE 3.10: Binary detection of object A at NTU's diving pool

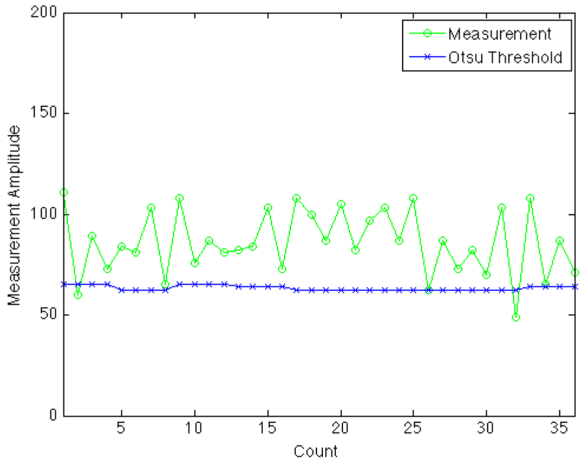

FIGURE 3.11: Binary detection of object B at NTU's diving pool

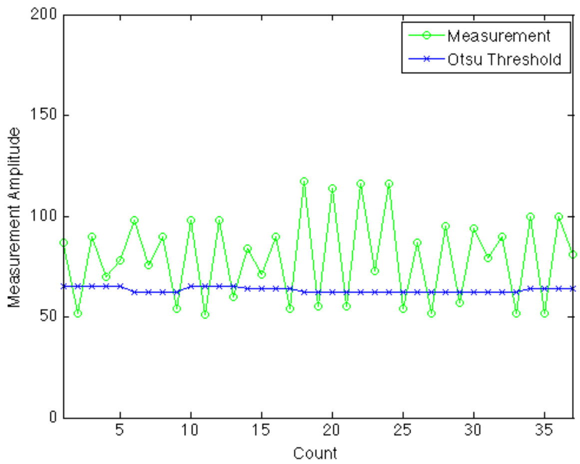

FIGURE 3.12: Binary detection of object C at NTU's diving pool

	Object		
	A	B	C
No. of Positive Detection	44	34	25
No. of Measurements	44	36	37
Percentage (%)	100	94	68

TABLE 3.2: Statistics of binary detection for the target points identified for NTU dataset

3.5 Static Thresholding

3.5.1 Background Statistics

Firstly, we analyze the statistics of the background noise that are free of objects. The background statistics from bin 15 to 17 are of concern as these are the bins where objects A, B and C lie. Note that from the 18th bin onwards in the selected sector is the statistics of the diving pool's left wall and multipath reflections. In Fig. 3.13, we can identify the sector to the left of the sonar image as a suitable sample dataset. The identified background sector is labelled with a red-colored arc. In Fig 3.14, it can be observed at bin 8 that there is a peak in the noise level. There is a ring of artifacts observed between the sonar and the objects as in Fig. 3.13.

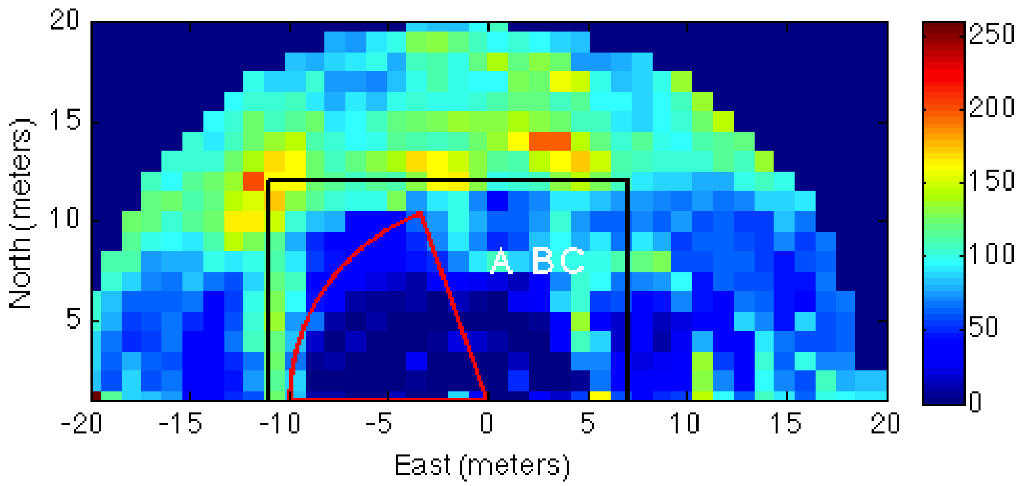

FIGURE 3.13: Background sector identified with the red-colored arc at NTU's diving pool

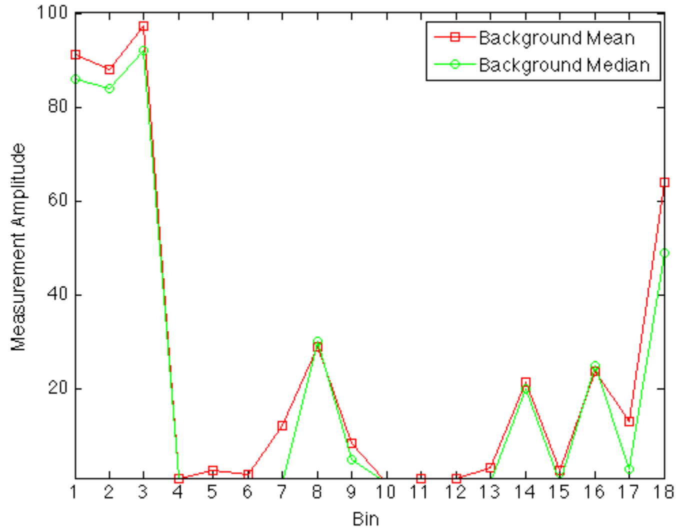

FIGURE 3.14: Background statistics of NTU's diving pool

Subsequently, assuming P_{FA} is set for 1% with the number of background statistics, N_i, as 196, the threshold constant K in (2.10) can be determined as:

$$\begin{aligned} K &= \sqrt{\left[(P_{FA})^{-\frac{1}{N_i}} - 1\right] N_i} \\ &= \sqrt{\left[(0.01)^{-\frac{1}{196}} - 1\right] 196} \\ &= 2.1586 \end{aligned} \tag{3.1}$$

3.5.2 Decision Statistic

The decision statistic $\tilde{S}$ of the objects at NTU's diving pool is estimated as in (2.1). In Fig. 3.15, we present the computed $\tilde{S}$ of all the objects.

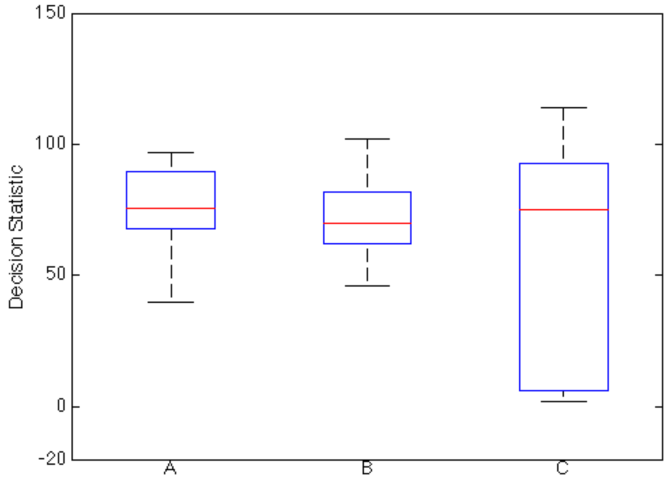

FIGURE 3.15: Decision statistic of the objects at NTU's diving pool

The $\tilde{S}$ for objects A and B range from 40 to 102. Objects A and B should have high P_T. However, object C has its $\tilde{S}$ ranging from 2 to 114. Object C might have several measurements that lead to low P_T. The computed median $\tilde{S}$ of all the objects is around 70. These should generally still lead to high P_T. The $\tilde{S}$ of the objects is summarized in Table 3.3.

Target	$\tilde{S}$		
	Min	Median	Max
A	40	75.5	97
B	46	70	102
C	2	75	114

TABLE 3.3: Statistics of $\tilde{S}$ for the objects at NTU's diving pool

3.5.3 Probability of Target

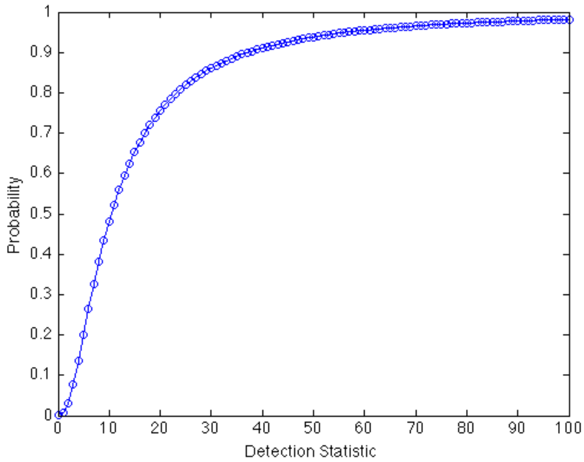

FIGURE 3.16: P_T for NTU dataset

Assuming P_{FA} is set for 1% with the number of background statistics, N_i, as 196, P_T in (2.12) is computed as in Fig. 3.16. Based on $\tilde{S}$ of the objects in Section 3.5.2, the measurements yield median P_T of more than 98%. These should lead to high P_O. Only object C has its P_T extending lower towards 21%. If there is a significant number of continuous measurements that lead to low P_T, object C might have low P_O. The P_T for the objects can be summarized as follows:

Target	P_T		
	Min	Median	Max
A	0.9702	0.9905	0.9941
B	0.9767	0.9891	0.9946
C	0.2122	0.9904	0.9957

TABLE 3.4: Statistics of P_T for the objects at NTU's diving pool

3.5.4 Occupancy Grid

The result of the occupancy grid is in Fig. 3.17. All the targets and the walls of the diving pools are 100% detected. Most of the artifacts between the sonar and the objects are filtered out using the static thresholding. The slope behind the objects is partially detected as there is a portion of the slope between the objects and the wall that is not detected. The portion of the frontal slope that is parallel to the sonar is 100% detected. However, the slope to portside of the sonar is not detected. In addition, the artifacts between the sonar and the objects are filtered off by the thresholding. There are also less artifacts observed beyond the boundary of the diving pool as compared to the result using Otsu thresholding in Fig. 3.9.

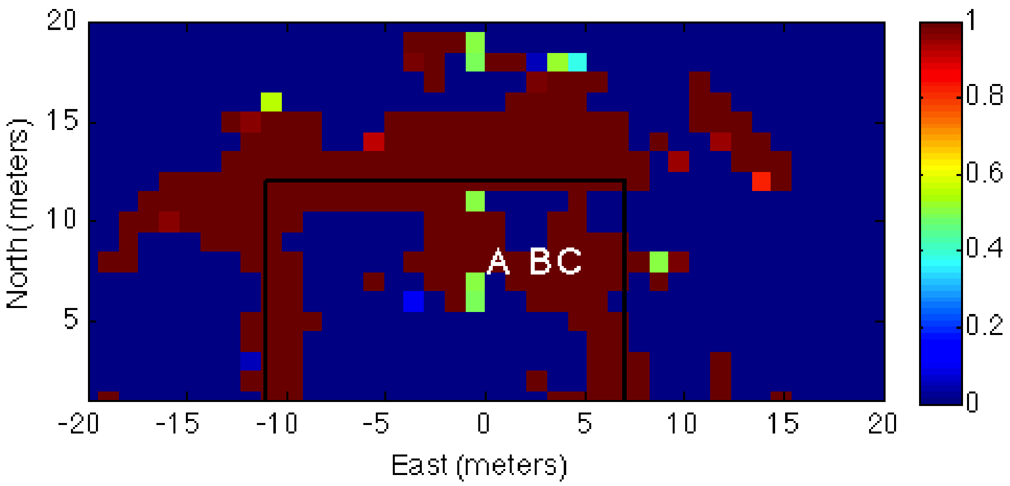

FIGURE 3.17: Result of occupancy grid with static thresholding for NTU dataset

We analyze the first 20 measurements of each objects against their respective $\tilde{S}$, P_T and P_O from Fig. 3.18 to Fig. 3.20. The P_T and P_O for objects A and B are high throughout. The fluctuations of $\tilde{S}$ for object C result in fluctuations of P_T. However, their P_O was high throughout as most of its initial measurements result in high P_T.

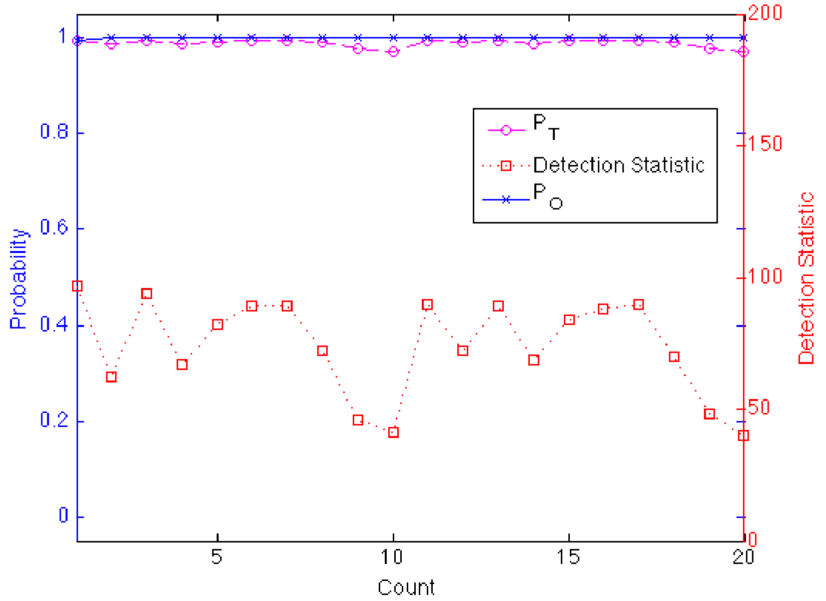

FIGURE 3.18: Plot of P_T, $\tilde{S}$ and P_O for object A at NTU's diving pool

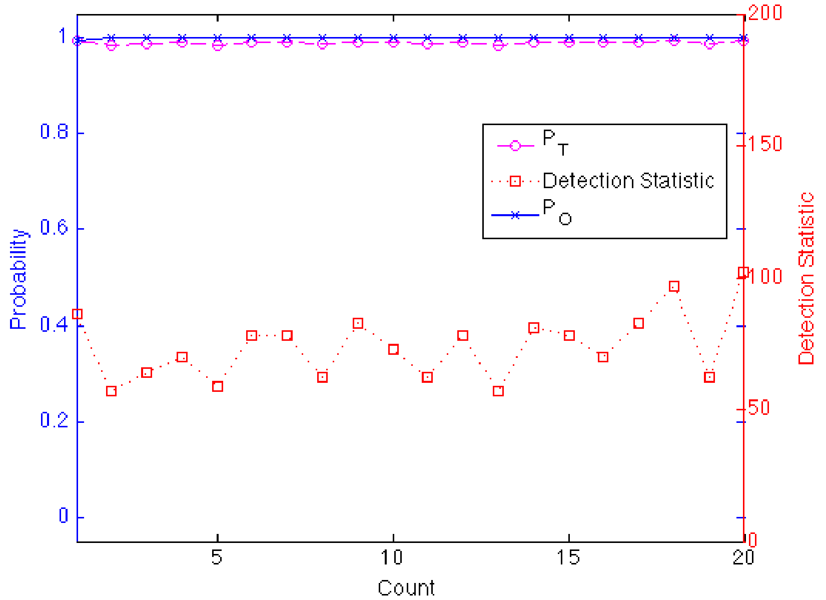

FIGURE 3.19: Plot of P_T, $\tilde{S}$ and P_O for object B at NTU's diving pool

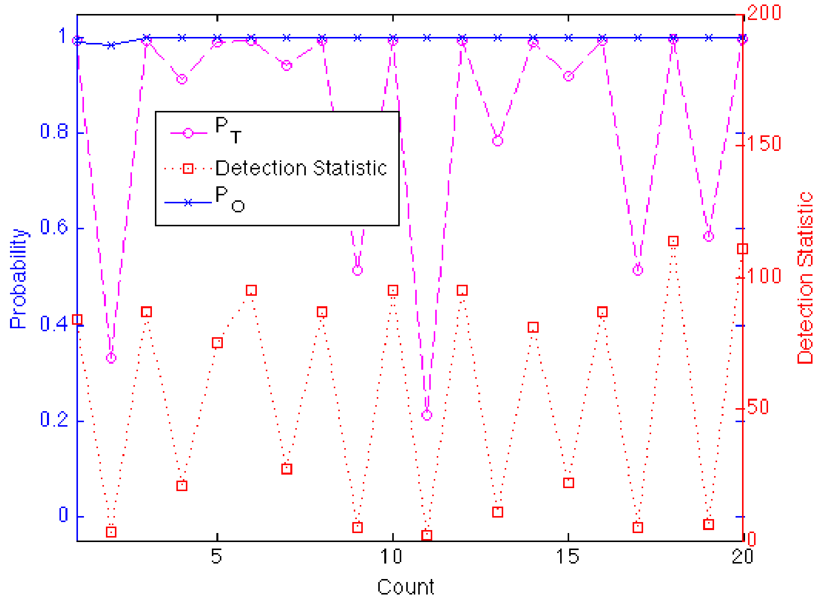

FIGURE 3.20: Plot of P_T, $\tilde{S}$ and P_O for object C at NTU's diving pool

3.6 Summary

The results and observations using Otsu thresholding and static thresholding can be summarized in Table 3.5.

<table>
<tr><th></th><th>Otsu Thresholding</th><th>Static Thresholding</th></tr>
<tr><td>Threshold</td><td>The median threshold determined over 9 iterations is at the value of 62.</td><td>Several spikes was observed for the background estimate. One of the initial spike is due to the ring of artifacts observed between the sonar and objects. The other spikes were near the boundary of the pool.</td></tr>
<tr><td rowspan="4">Detection</td><td>Objects A, B and C respectively have mean detection of 100%, 94% and 68%.</td><td>Objects A, B and C have median P_T of more than 98% that results in P_O of 100%.</td></tr>
<tr><td colspan="2">All the walls are detected.</td></tr>
<tr><td colspan="2">The portion of the frontal slope parallel to the sonar was 100% detected.</td></tr>
<tr><td colspan="2">The artifacts between the sonar and the objects were filtered off by the threshold.</td></tr>
<tr><td>Others</td><td>Several scanline measurements have to be collated to form a sectorial image. In a static setup, it is easy to collate the scanline measurements.</td><td>Background sector was difficult to identify. The background sector might have objects that can cause inaccurate background estimate.</td></tr>
</table>

TABLE 3.5: Summary of detection methods for NTU dataset

Chapter 4

Experimental Data — Static Setup at RSYC

4.1 Experimental Setup

An experiment with the Micron DST sonar was conducted at Republic of Singapore Yacht Club (RSYC) to investigate the measurement statistics of objects detection. RSYC serves as a marina for vessels of various sizes. Although it is situated next to a busy ferry port and an open-water anchoring site with quite a busy waterway, the inner area of the marina should still be rather calm for objects detection with the sector scanning sonar. Another key consideration is that the marina truly serves as an environment where AUVs can be operationally deployed. It is in such environments where objects detection and avoidance plays a critical factor in ensuring a safe operation for the AUVs. An overlay of a sonar image on the satellite view of the potential objects can be seen in Fig. 4.1.

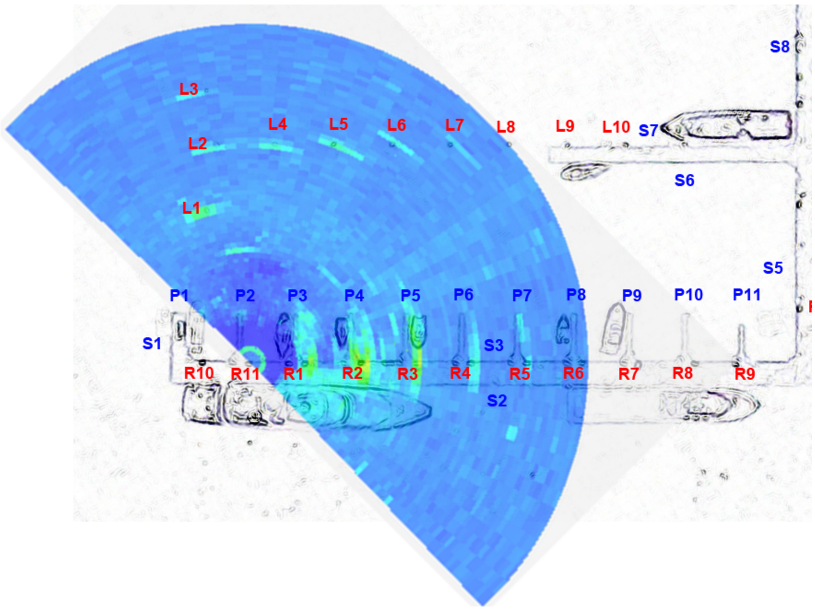

FIGURE 4.1: Overlay of FLS image with satellite view of potential objects at RSYC

Objects with a prefix 'S' are vessels that are present at the marina during the experiment. These are not objects intended to be ensonified. However, the draft and bottom-hull of these vessels might be ensonified and appear as significant objects in the measurements. Objects with a prefix 'P' are pier structures at the marina. These pier structures are of floating structures and should not appear as significant objects in the measurements. These pier structures are actually supported by rigid beams labelled with prefixes 'L' and 'R'. The objects with a prefix 'L' and 'R' are respectively to the left and right of the sonar. These objects should easily be ensonified and appears as significant objects in the measurements.

The sonar was placed at 3m depth with the estimated depth of the test site is ∼6m. The ensonification range was configured for 75m with 65 measurement bins. Along with a vertical beamwidth of 35°, the sonar signal will hit the water surface or the bottom at the horizontal distance of ∼9.5m from the sonar or at the 11th measurement bin. It is expected that the measurements will be affected by reverberations.

4.2 Measurement Statistics

The measurements of the objects with prefixes 'L' and 'R' are presented in Fig. 4.2. As the objects are farther away from the sonar, their measurements can be observed to be reducing in amplitude.

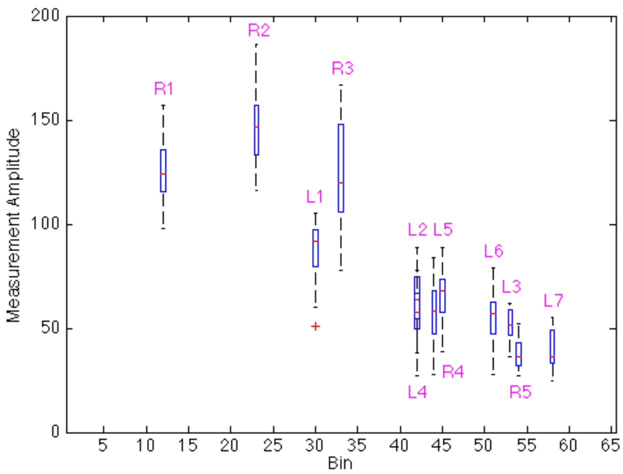

FIGURE 4.2: Measurements of the objects at RSYC

4.3 Receiver Operating Characteristic

Based on the measurements of the objects in Fig. 4.2, we can attain the ROC curves for the objects as presented from Fig. 4.3 to Fig. 4.6. Object L1 to L6 along with R1, R2 and R3 have desirable ROC curves where high P_D can be achieved with rather low P_{FA}. As objects are farther away, their ROC curves become less desirable. This can be observed for R4 and R5 that have less desirable ROC curves compared to L1. L7 is farthest away and has a linear ROC curve that implies a random guess of detection. All objects except for L7 should have good performance with the detector.

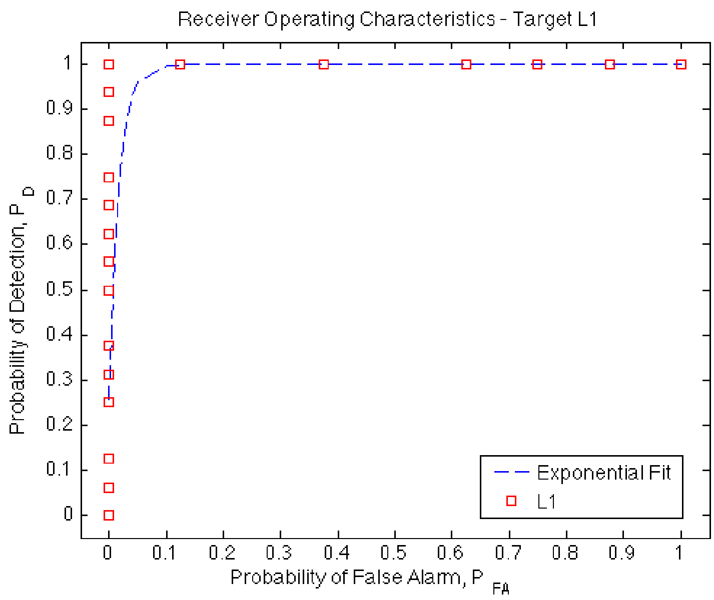

FIGURE 4.3: ROC of object L1 at RSYC[1]

[1]The fit used is $P_D = 1 + [-0.7569 \times \exp(-59.16 \times P_{FA})]$.

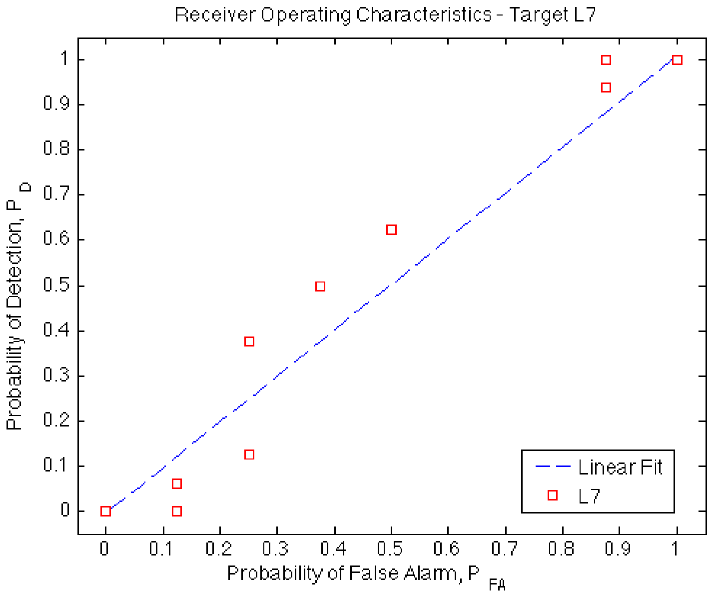

FIGURE 4.4: ROC of object L7 at RSYC[2]

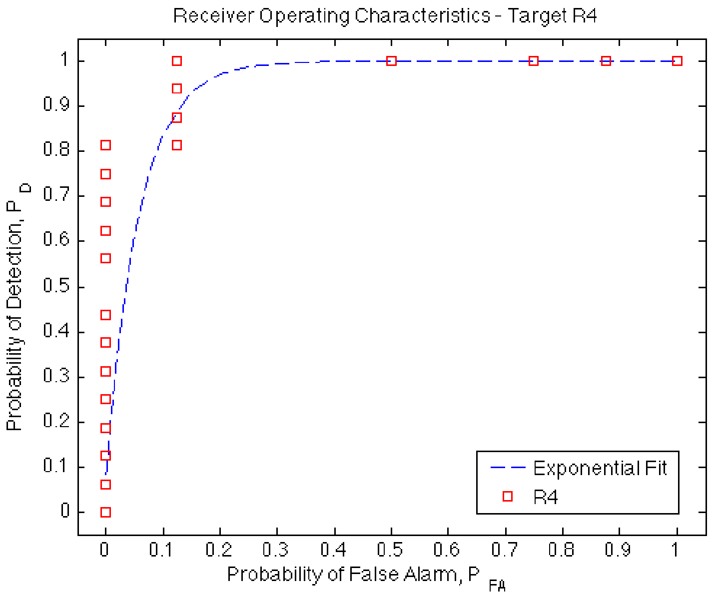

FIGURE 4.5: ROC of object R4 at RSYC[3]

[2]The fit used is $P_D = P_{FA}$.
[3]The fit used is $P_D = 1 + [-0.9282 \times \exp(-17.48 \times P_{FA})]$.

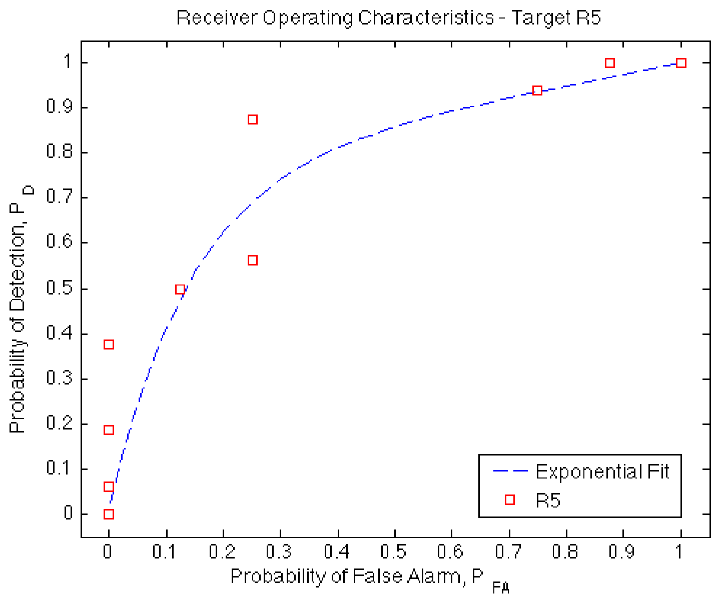

FIGURE 4.6: ROC of object R5 at RSYC[4]

4.4 Otsu Thresholding

The Otsu threshold in (2.8) is computed based on the statistics of several scanline measurements that were collated to form a sectorial image. We collated 30 scanline measurements to form the first sectorial image with a field of view of 90°. This is because the sector scanning sonar begins its ensonification looking ahead followed with a 90° rotation towards the starboard. Subsequently, we collated 60 scanline measurements to form a sectorial image with a field of view of 180° that spans all the way from starboard of the sonar till its portside. There were 18 iterations and the

[4]The fit used is $P_D = [0.7762 \times \exp(0.2553 \times P_{FA})] + [-0.765 \times \exp(-6.943 \times P_{FA})]$.

thresholds determined are presented in Fig. 4.7. The median threshold determined is at the value of 47.

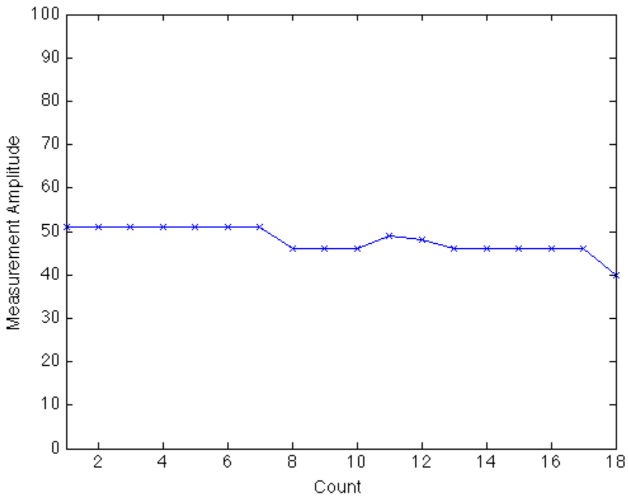

FIGURE 4.7: Otsu threshold for RSYC dataset

4.4.1 Binary Occupancy Grid

The mean result of the binary occupancy grid is in Fig. 4.8. Object L7 that is farthest away from the sonar is not detected using Otsu thresholding with a mean result of 0%. R5 is the second farthest object and it is barely detected with a mean detection of 8%. All other objects are easily detected with mean detection exceeding 50%. L1, R1, R2 and R3 have a mean detection of 100%. The mean detection decreases as the object is farther away. R4 and R5 that are farther away from R1, R2 and R3 have a mean detection of 76% and 8%. L2 to L6 have mean detection ranging from 68% to 93%. The results of the mean detection described earlier for object

L1 to L6 is based on a specific grid cell. In Fig. 4.8, we observe that there is annular spreading of the measurements for the objects. Those measurements are with mean detection at 100%. This implies that objects can still be easily detected. However, objects L7 and R5 that are farther away still have lower measurements that might impede their detection.

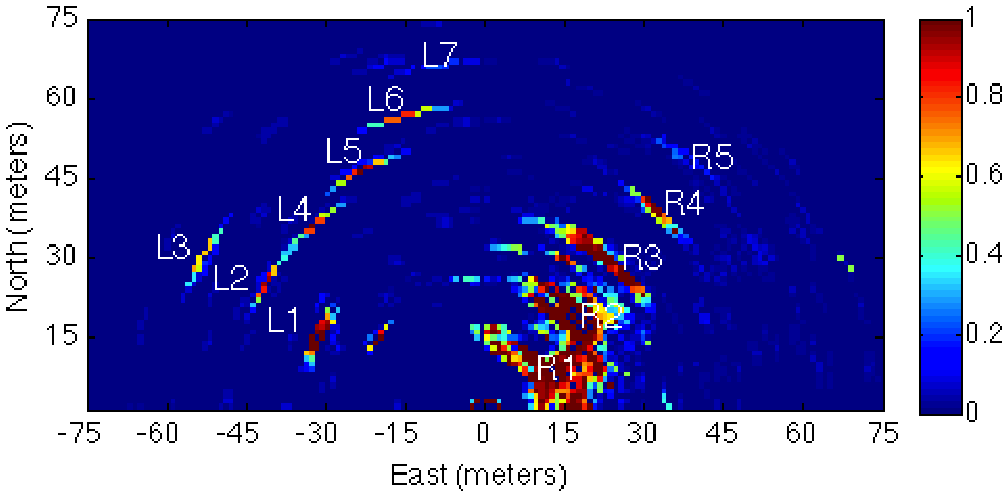

FIGURE 4.8: Mean result of the binary occupancy grid with Otsu thresholding for RSYC dataset

In Fig. 4.9 to Fig. 4.13, we analyze the measurements of the objects against their respective Otsu threshold to understand the results of binary detection.

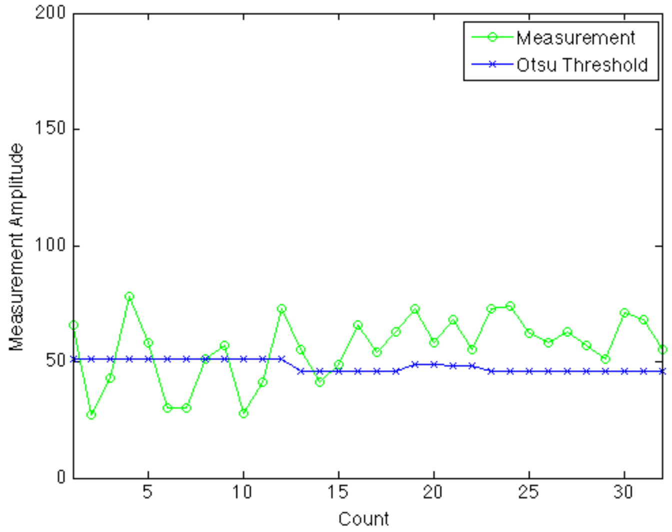

FIGURE 4.9: Binary detection of object L4 at RSYC

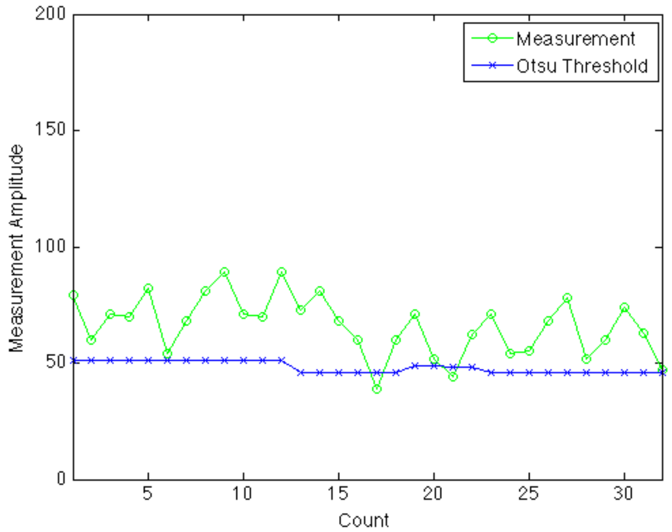

FIGURE 4.10: Binary detection of object L5 at RSYC

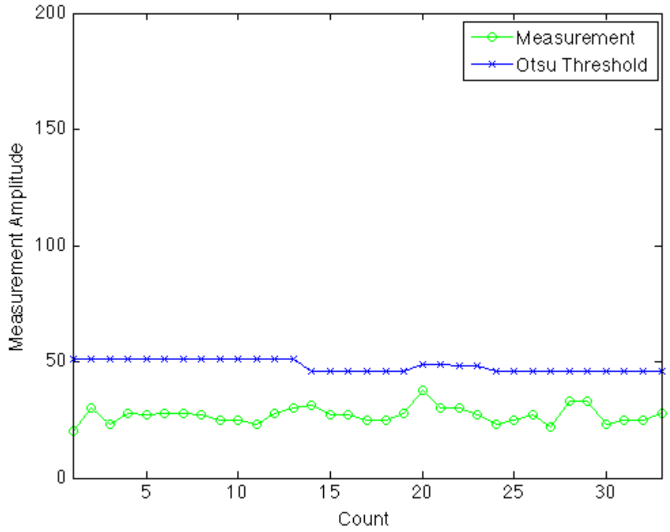

FIGURE 4.11: Binary detection of object L7 at RSYC

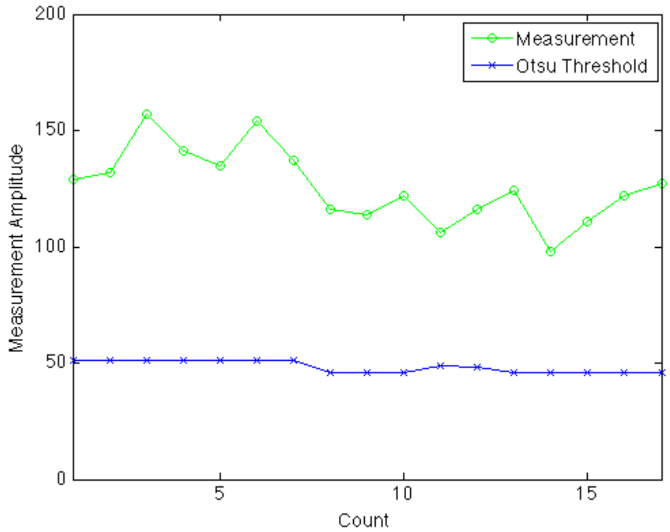

FIGURE 4.12: Binary detection of object R1 at RSYC

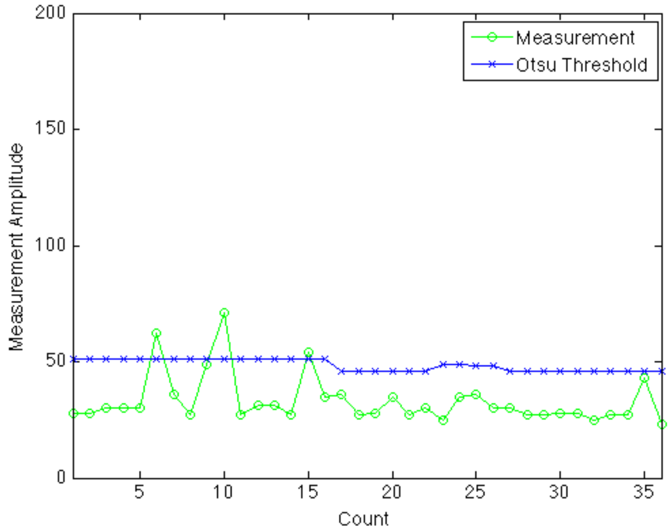

FIGURE 4.13: Binary detection of object R5 at RSYC

The observations made on the binary detection of the objects are as follows:

L1, L2, L3, L5	Most measurements are higher than the threshold with some measurements being marginally close to the threshold.
L4, L6, R4	Most measurements are higher than the threshold but some measurements are lower than the threshold.
L7	All the measurements are lower than the threshold. L7 isn't detected using the Otsu threshold.
R1, R2, R3	All the measurements exceed the threshold.
R5	Most measurements are lower than the threshold with only several measurements exceeding the threshold. R5 isn't detected using the Otsu threshold.

4.5 Static Thresholding

4.5.1 Background Statistics

Firstly, we analyze the statistics of the background noise that are free of objects. In Fig. 4.14(a), we can identify the sector to the left of the sonar image as a suitable sample dataset.

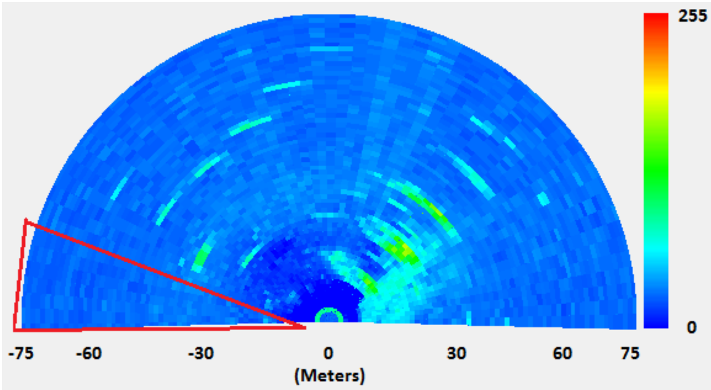

(a) Background sector

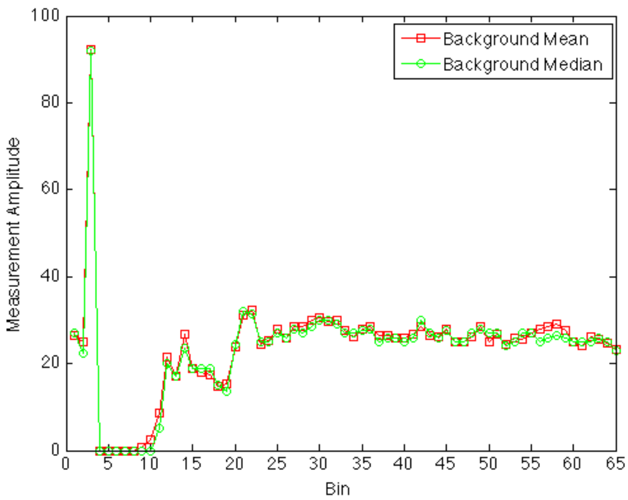

(b) Background statistics

FIGURE 4.14: Background noise of RSYC

In Fig. 4.14(b), a spike corresponding to the transmission of the sonar ping can be observed at bin 3. The amplitude of the measurement is gradually increasing from the 9th bin until the 30th bin. This corresponds to where reverberations are expected as the sonar was only placed at 3m depth while the depth of the test site is ∼6m. After the 30th bin, the background statistics is rather constant throughout. There are also some spikes observed between bin 12 to 15. These are indications that there are potential objects in those bins or there are higher intensity returns from the noise clutter.

Assuming P_{FA} is set for 1% with the number of background statistics, N_i, as 8, the threshold constant K in (2.10) can be determined as:

$$\begin{aligned} K &= \sqrt{\left[(P_{FA})^{-\frac{1}{N_i}} - 1\right] N_i} \\ &= \sqrt{\left[(0.01)^{-\frac{1}{8}} - 1\right] 8} \\ &= 2.4952 \end{aligned} \tag{4.1}$$

4.5.2 Decision Statistic

The decision statistic $\tilde{S}$ of the objects at RSYC is estimated as in (2.1). In Fig. 4.15, we present the computed $\tilde{S}$ of all the objects. R1, R2 and R3 are objects that are less than 40m away from the sonar with median detection statistic of more than 100. L1 is also less than 40m away but its median detection statistic is only around 60. These objects are expected to easily have high P_T. L2, L4, L5, L6 and R4 are objects with decision statistic ranging between 0 and 61 with a median of around 30. These objects should still have high P_T.

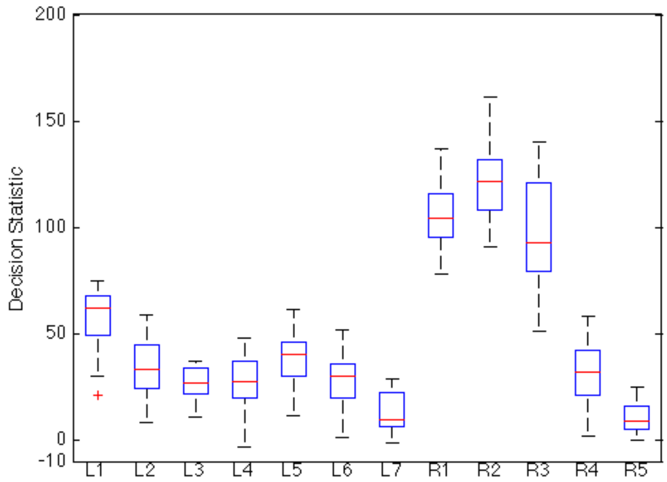

FIGURE 4.15: Decision statistic of the objects at RSYC

L4 also has several decision statistic at 0 and negative decision statistic. Since most of the decision statistic is more than 20, L4 should still have high P_T. R5 has several detection statistic nearing and at 0 while L4 and L7 have several negative detection statistic. This is because we were conservative when we considered the median background statistics as the background estimate. L3 and R5 are almost at the same distance but the decision statistic for L3 is slightly higher than R5. This means that L3 is likely to have higher P_T than R5. Besides that, the fluctuations for L4 encompasses the fluctuations for R5. However, most of the detection statistic for L4 is more than 25 but it is mostly less than 25 for R5. This means that L4 is still likely to have higher P_T than R5. Since L4 have several negative detection statistic, L4 might have lower P_T than R5 if the last few remaining detection statistic near 0 or becomes negative.

4.5.3 Probability of Target

Assuming P_{FA} is set for 1% with the number of background statistics, N_i, as 8, P_T in (2.12) is computed as in Fig. 4.16.

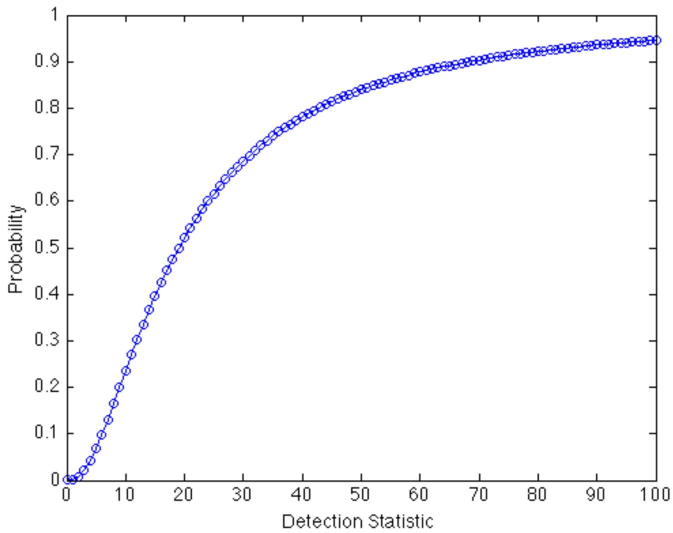

FIGURE 4.16: P_T for RSYC dataset

Based on the decision statistic of the objects as in Fig. 4.15, the P_T for all the objects can be summarized as in Fig. 4.17. The observations made earlier in Section 4.5.2 about the P_T for objects L1, R1, R2 and R3 are as expected. All other objects have P_T ranging from 1% to 90%. Objects L2, L3, L4, L5, L6 and R4 have most of the P_T more than 75%. L7 and R5 that are farther away also have P_T ranging from 1% to 78% even though their decision statistic was generally less than 30. This is because P_T goes up rapidly with $\tilde{S}$ and then saturates. The distribution of their P_T seems rather spread out. All the objects except for L7 and R5 should then have high P_O. Objects L7 and R5 might have low P_O.

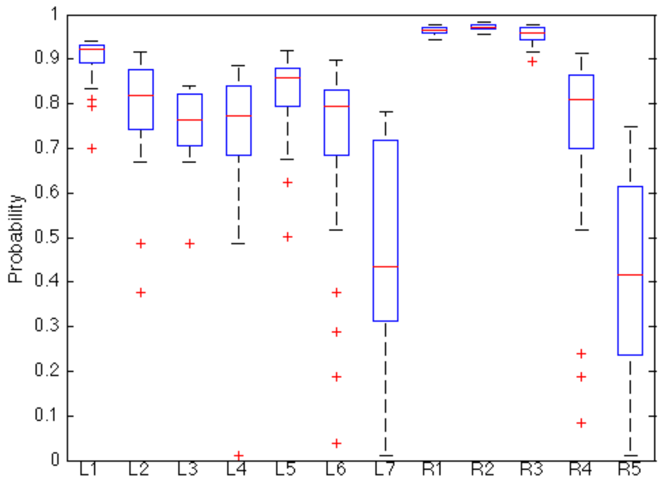

FIGURE 4.17: P_T of the objects at RSYC

4.5.4 Occupancy Grid

The result of the occupancy grid is in Fig. 4.18. All the objects are detected with P_O of 100%. However, there were more artifacts observed to the starboard of the sonar.

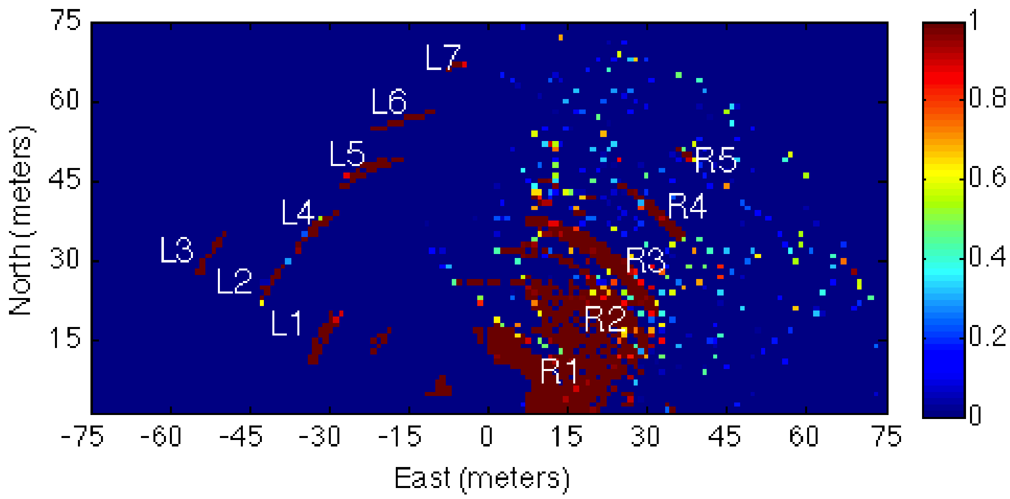

FIGURE 4.18: Result of occupancy grid with static thresholding for RSYC dataset

We analyze the measurements of the objects against their respective $\tilde{S}$, P_T and P_O from Fig. 4.19 to Fig. 4.25.

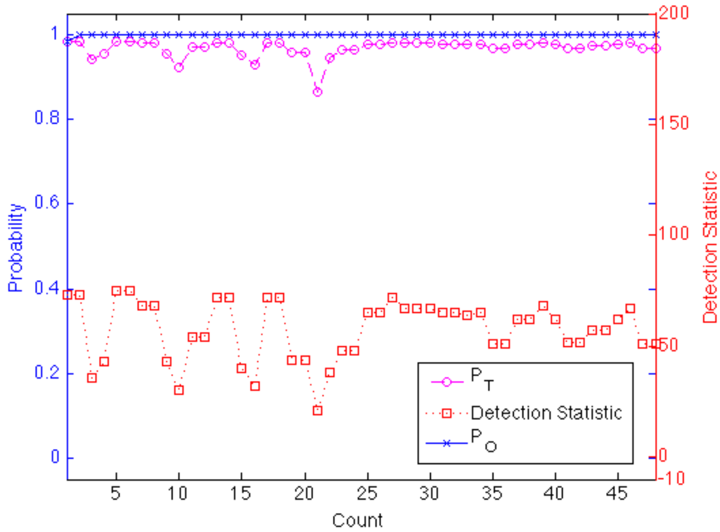

FIGURE 4.19: Plot of P_T, $\tilde{S}$ and P_O of object L1 at RSYC

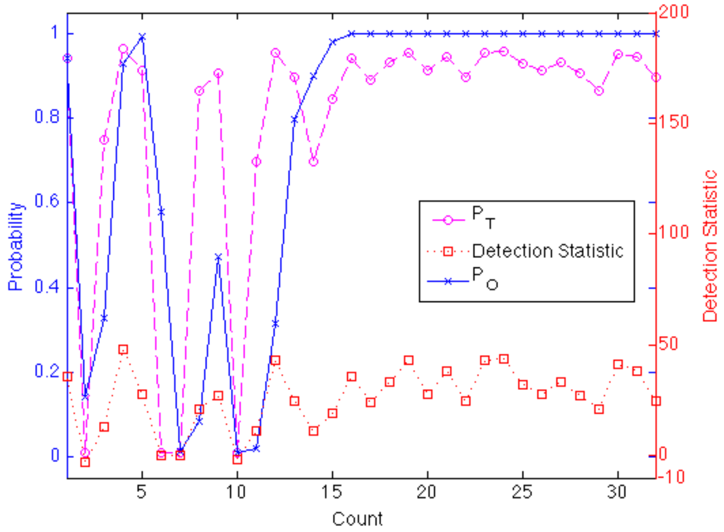

FIGURE 4.20: Plot of P_T, $\tilde{S}$ and P_O of object L4 at RSYC

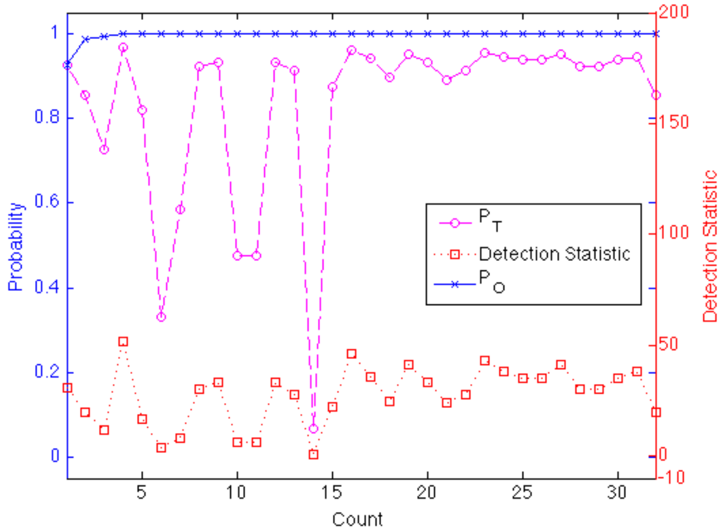

FIGURE 4.21: Plot of P_T, $\tilde{S}$ and P_O of object L6 at RSYC

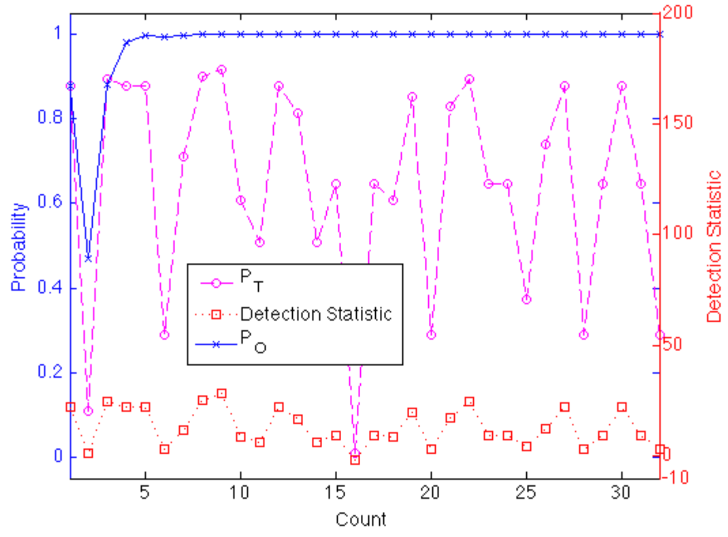

FIGURE 4.22: Plot of P_T, $\tilde{S}$ and P_O of object L7 at RSYC

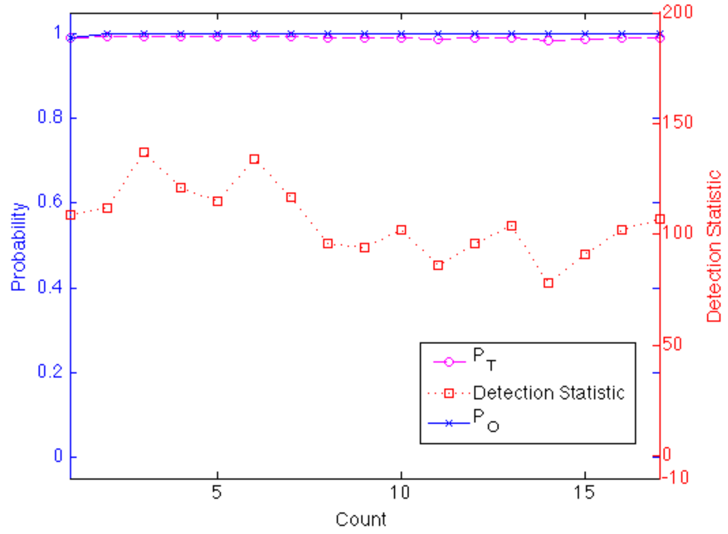

FIGURE 4.23: Plot of P_T, $\tilde{S}$ and P_O of object R1 at RSYC

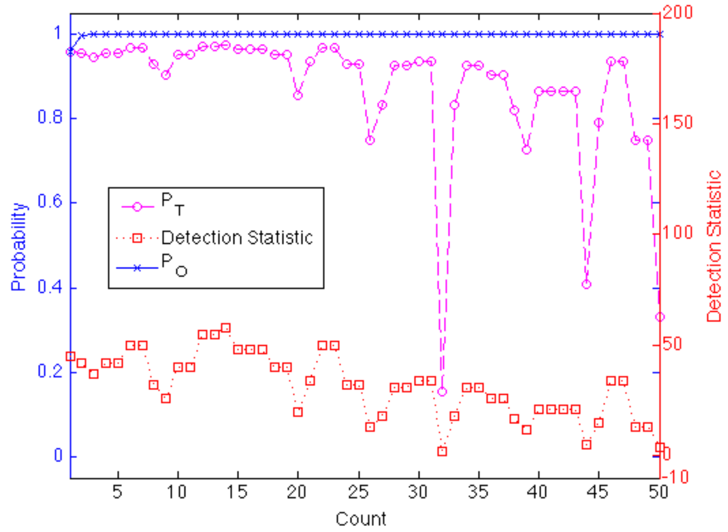

FIGURE 4.24: Plot of P_T, $\tilde{S}$ and P_O of object R4 at RSYC

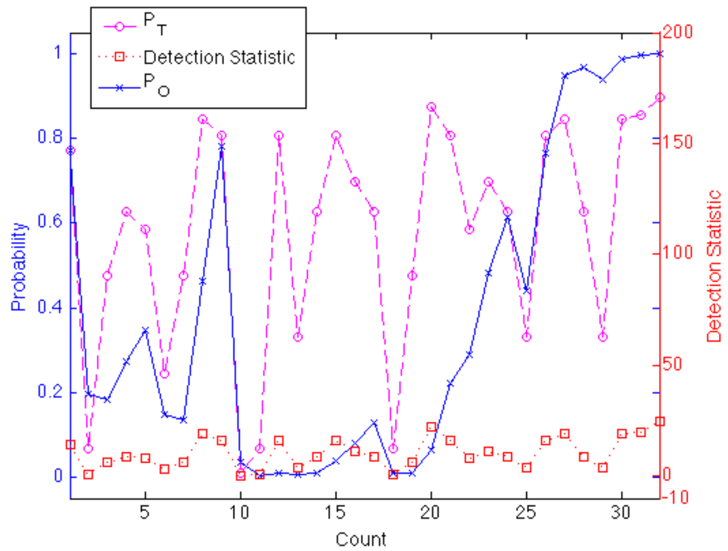

FIGURE 4.25: Plot of P_T, $\tilde{S}$ and P_O of object R5 at RSYC

The observations made on the $\tilde{S}$, P_T and P_O are as follows:

L1 The detection statistic average more than 50. This results in P_T exceeding 80% and P_O remains high throughout.

L2, L5, R4	The detection statistic fluctuates between 0 and slightly more than 50. Although there is a slowly decreasing trend with the decision statistic and P_T, several of the initial decision statistic already resulted in high P_O that subsequently remained high throughout.
L3	The detection statistic gradually increases nearing 40 and eventually fluctuates around 30. P_O gradually increases and remains high throughout.
L4	The detection statistic initially increases but there was a sudden decrease. The decrease resulted in very low P_T. After the 10th measurement, the detection statistic gradually increases nearing 40. P_T and P_O eventually became high.
L6	The detection statistic initially fluctuates between 1 and 50. These result in fluctuations for P_T ranging from 5% to 95%. The detection statistic gradually increases nearing 50. Several initial decision statistic resulted in high P_O that subsequently remained high throughout.
L7	The detection statistic range from marginally near 0 to 30. Several of the initial decision statistic were close to 20 and these resulted in P_T of more than 80%. P_O remained high throughout because there were subsequent decision statistic that results in high P_T.
R1, R2, R3	The detection statistic throughout was with a mean of 100. P_T and P_O remain high throughout.
R5	The detection statistic fluctuates between 0 and 25. After the 18th measurement, the decision statistic was slowly increasing. These result in several high P_T and P_O eventually became high.

4.6 Summary

Both approaches were able to detect all the objects except for Otsu thresholding that was unable to detect L7 and R5 that are farther away with measurements marginally near the background noise level. The Otsu thresholding yields a cleaner image compared to the result based on the static thresholding. There were artifacts observed in the starboard of the sonar using static thresholding. However, this was consistent with the statistics of the actual measurements. The results and observations using Otsu thresholding and static thresholding can be summarized in Table 4.1.

	Otsu Thresholding	Static Thresholding
Threshold	The median threshold determined over 18 iterations is at the value of 47.	The background estimate gradually increases with several spikes before it becomes constant throughout.
Detection	The result is very clean where there is almost no artifacts.	Artifacts are observed to the starboard of the sonar.
	All the objects except for L7 and R5 are detected.	All the objects are detected with P_O of 100%.
Others	Several scanline measurements have to be collated to form a sectorial image. In a static setup, it is easy to collate the scanline measurements.	Background sector was difficult to identify. The background sector might have objects that can cause inaccurate background estimate.

TABLE 4.1: Summary of detection methods for RSYC dataset

Chapter 5

Experimental Data — Dynamic Setup at Pandan Reservoir

5.1 Experimental Setup

An experiment with the Micron DST sector scanning sonar integrated on STARFISH AUV was conducted at Pandan Reservoir. This experiment involves a dynamically moving AUV scanning for static buoys and the reservoir's embankments. The sonar was configured for a 50m range with 44 bins. The AUV was operating at a constant depth of 0.5m while the depth of operating area varies between 2m and 6m. The overlay of the sonar rendering on top of the satellite view of the reservoir can be seen in Fig. 5.1. As the AUV is heading towards the embankments, there is an area in front of the AUV with measurements of high amplitude. The first measurement of ∼150 is the lower embankment wall of the reservoir. This lower embankment wall is submerged and is not visible from the surface. The second measurement of ∼150 is the upper embankment wall that is near the surface and the walkway is visible on the satellite image. The depiction of the embankments at Pandan Reservoir is in Fig. 5.2.

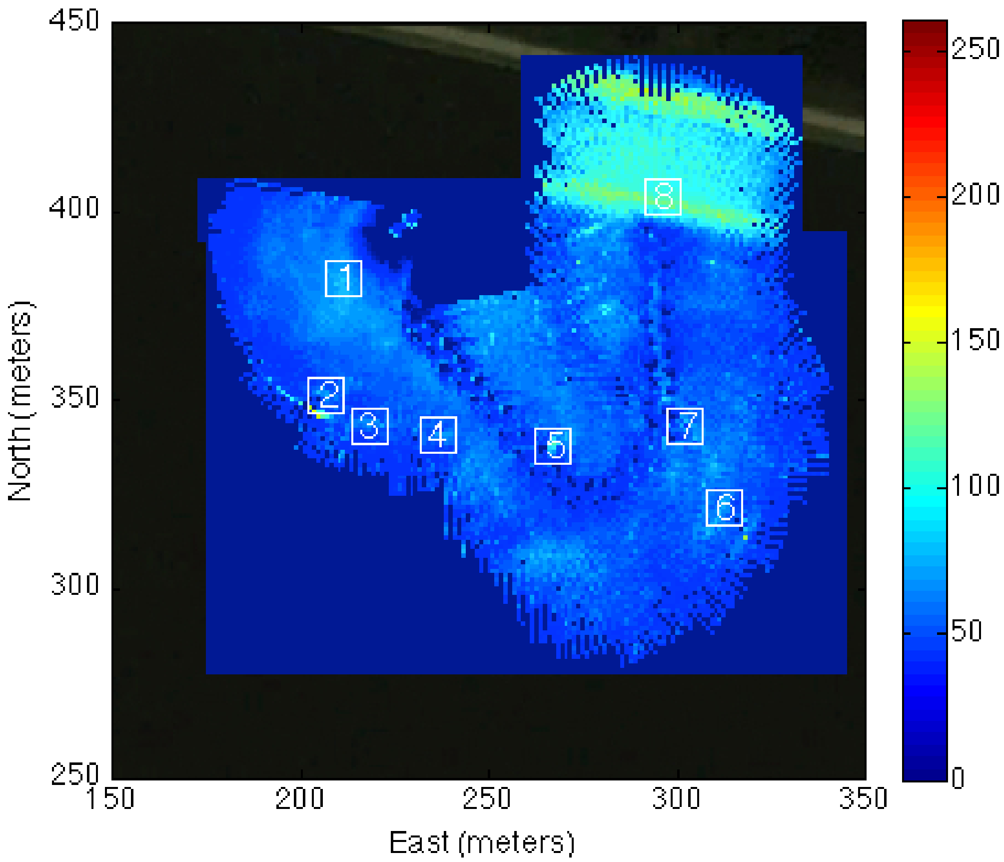

FIGURE 5.1: Overlay of the sonar rendering of Pandan Reservoir along with the target points

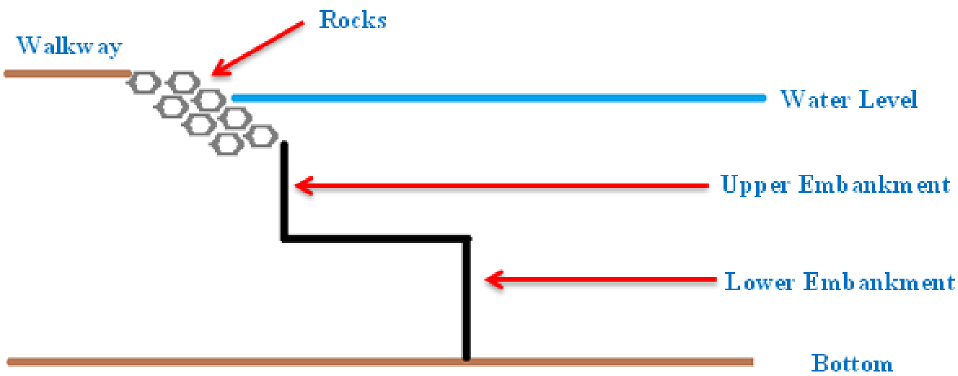

FIGURE 5.2: Depiction of the embankments at Pandan Reservoir

5.2 Measurement Statistics

We analyze the statistics of the target points in Fig. 5.1. Point 8 is the lower embankment wall detected at the reservoir. All other points are static demarcation buoys at the reservoir. Most of the measurements are exceeding 50 except for Point 5 and 7 that have several measurements below 50. The AUV was in motion throughout the mission and the ensonification of the target points could occur from varying distances and bearings. The measurements of the target points are categorized according to their respective object as in Fig. 5.3. If we were to plot the measurements against bin, the representation is inaccurate because measurements at different bins have differing annular statistics, propagation loss and processing gain. The statistic of the measurements are also summarized in Table 5.1.

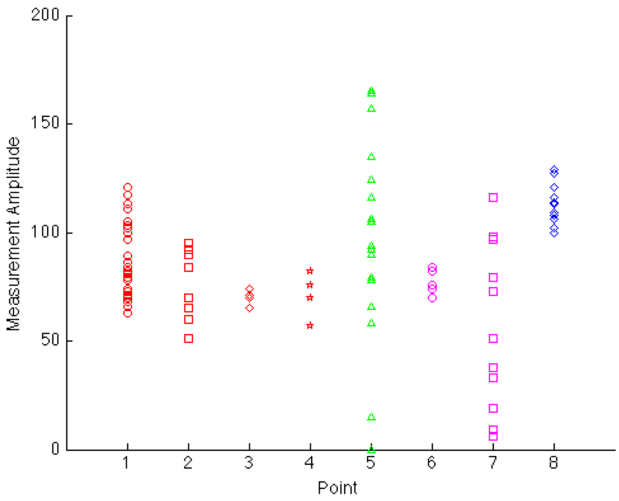

FIGURE 5.3: Measurements of the target points identified at Pandan Reservoir

Measurement	Point							
	1	2	3	4	5	6	7	8
Min	63	51	65	57	0	70	6	100
Median	81.5	77	70.5	70	92	75	44.5	113.5
Max	121	95	74	82	165	84	116	129

TABLE 5.1: Measurement statistics of the target points identified at Pandan Reservoir

5.3 Otsu Thresholding

The Otsu threshold in (2.8) is computed based on the statistics of several scanline measurements that were collated to form a sectorial image. During the start of the mission run till about the 1000th scanline measurement, we collated 100 scanline measurements to form the sectorial image with a field of view of 90°. This is because the AUV was still cruising at a straight path from the start of the mission run till about the 1000th scanline measurement. Subsequently, the AUV was making a turn towards the embankments before maintaining a straight path heading again. We then collated 50 scanline measurements to form the sectorial image with a field of view of about 70°. There were 44 iterations and the thresholds determined are presented in Fig. 5.4. The median threshold determined is at the value of 33. There is an increase of the threshold nearing the 40th iteration. This is because the AUV was heading straight towards the embankments that are of high amplitude.

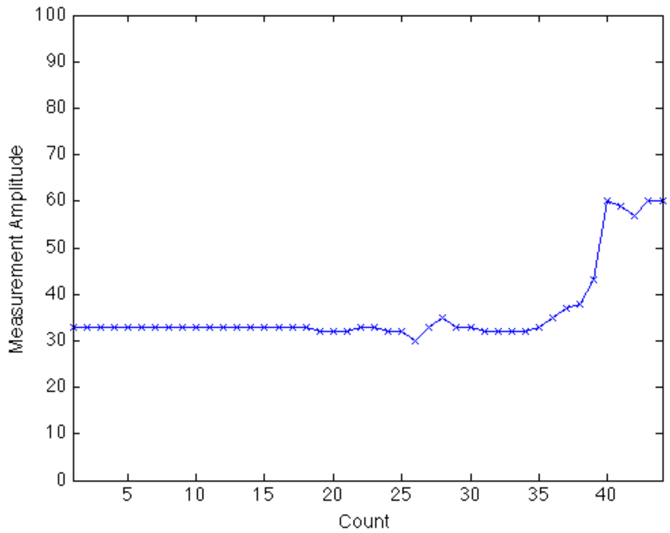

FIGURE 5.4: Otsu threshold for Pandan Reservoir dataset

5.3.1 Binary Occupancy Grid

The result of the median grid cells is in Fig. 5.5. The result is highly undesirable as all the measurements are considered as objects. This is because the most of the measurements evaluated for each sectorial image exceed the Otsu threshold. The statistic of the measurements for each sectorial image is depicted in Fig. 5.6.

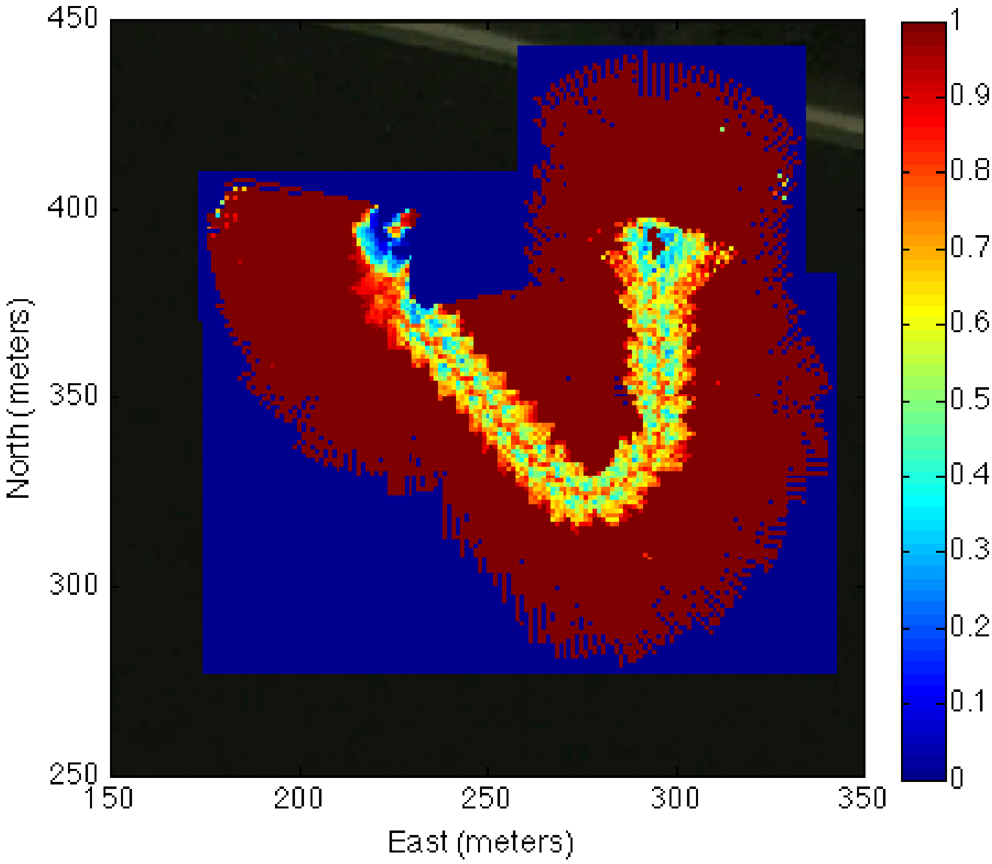

FIGURE 5.5: Mean result of the binary occupancy grid with Otsu thresholding for Pandan Reservoir dataset

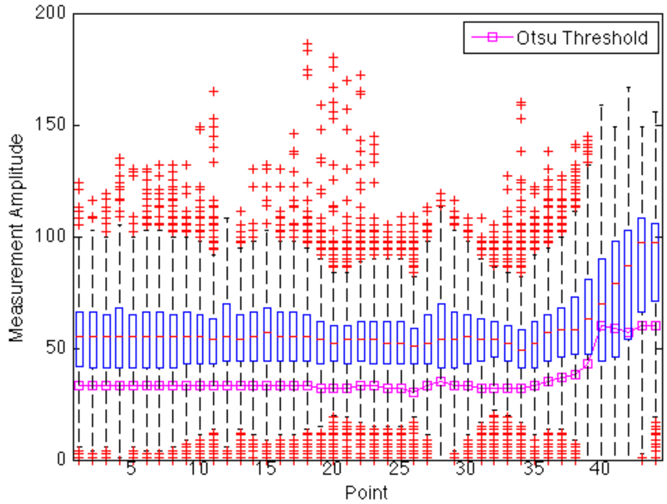

FIGURE 5.6: Measurement statistic of the sectorial image using boxplot against the Otsu threshold for Pandan Reservoir dataset

5.4 Static Thresholding

5.4.1 Background Statistics

Firstly, we analyze the statistics of the background noise that are free of targets. In Fig. 5.7, we can identify the sector during the initialization of the mission to understand the statistics of the background noise. In Fig. 5.8, we can observe that the median statistics of the background sector is higher than that of RSYC and NTU. The median statistics are significantly higher from the bin 10 onwards. These could be due to the water surface's wakes that results in higher amplitude as the AUV was only operating at the depth of 0.5m.

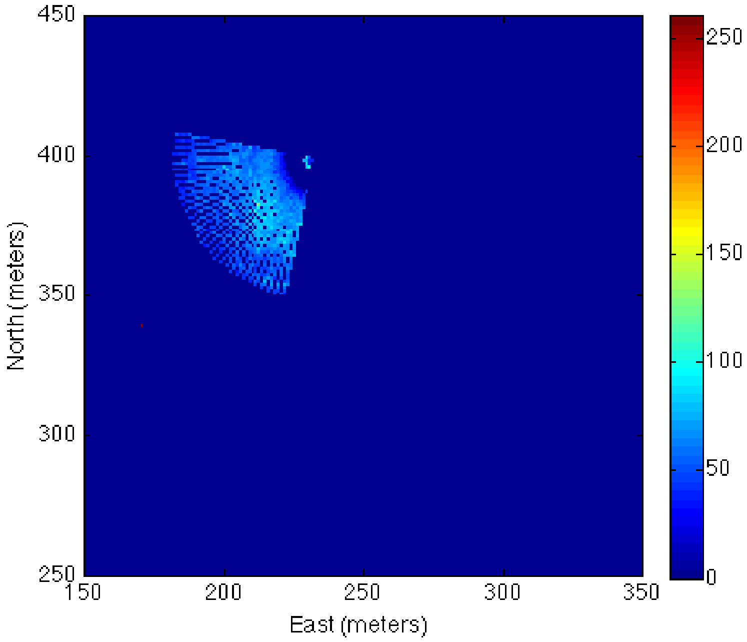

FIGURE 5.7: Background sector identified for Pandan Reservoir dataset

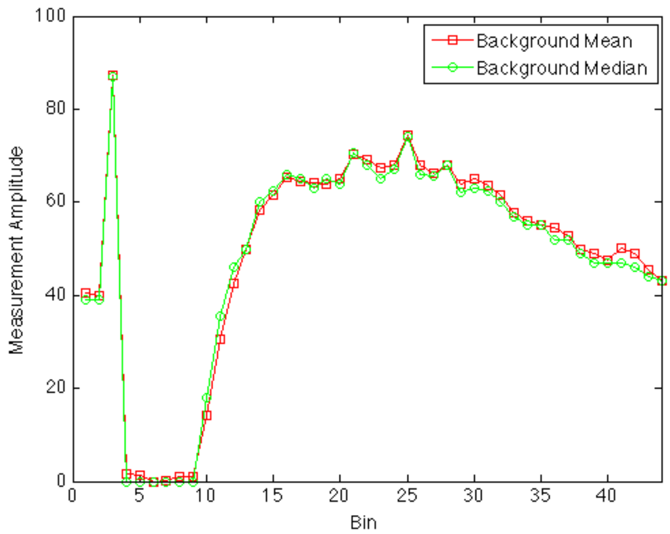

FIGURE 5.8: Background noise of Pandan Reservoir

Subsequently, assuming P_{FA} is set for 1% with the number of background statistics, N_i, as 50, the threshold constant K in (2.10) can be determined as:

$$\begin{aligned} K &= \sqrt{\left[(P_{FA})^{-\frac{1}{N_i}} - 1\right] N_i} \\ &= \sqrt{\left[(0.01)^{-\frac{1}{50}} - 1\right] 50} \\ &= 2.1963 \end{aligned} \tag{5.1}$$

5.4.2 Decision Statistic

The decision statistic $\tilde{S}$ of the target points at Pandan Reservoir is estimated as in (2.1). The computed $\tilde{S}$ of all the objects are depicted in Fig. 5.9.

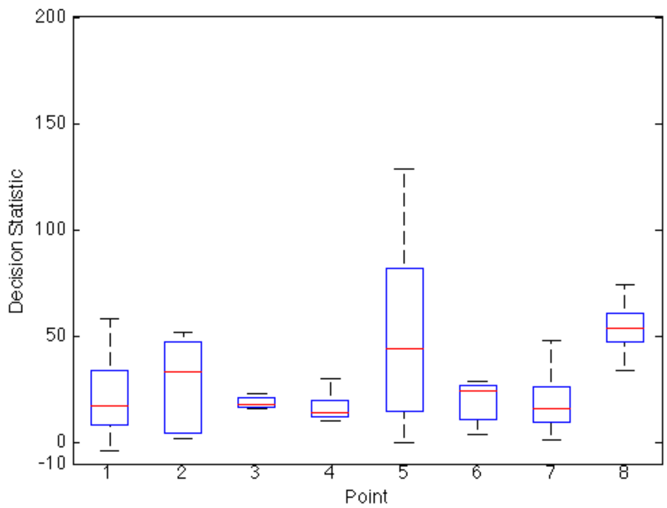

FIGURE 5.9: Decision statistic of the target points identified at Pandan Reservoir

The decision statistic for all the target points are mostly between 0 and

50. Only point 5 and 8 have several decision statistic with higher value. Point 8 should easily have high P_T as its $\tilde{S}$ ranges from 34 to 74. Point 8 is actually the reservoir's embankment. Therefore, it is expected that it should be detected. Point 5 might end up with a low P_T because it also has several $\tilde{S}$ that are of lower value. All other target points might be able to attain P_T with the value of around 80% as their median $\tilde{S}$ is around the value of 25.

5.4.3 Probability of Target

Assuming P_{FA} is set for 1% with the number of background statistics, N_i, as 50, P_T in (2.12) is computed as in Fig. 5.10.

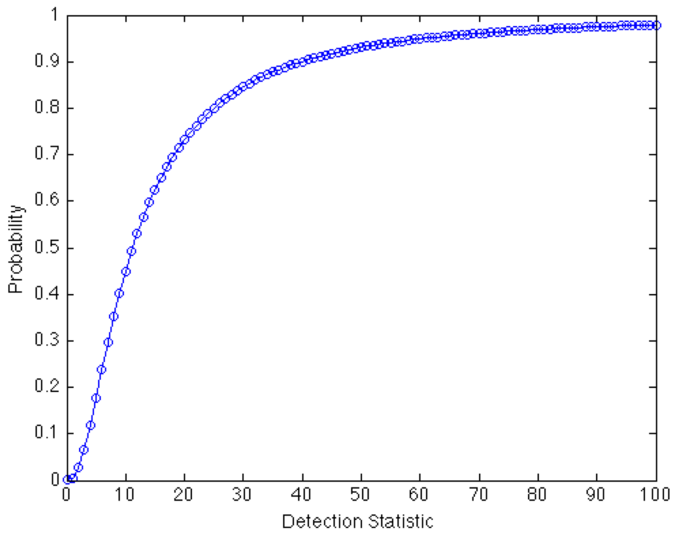

FIGURE 5.10: P_T for Pandan Reservoir dataset

Based on the decision statistic of the targets as in Fig. 5.9, the P_T for all the target points can be summarized in Fig 5.11 and Table 5.2. Point 8 has a concentration of P_T of at least 95%. This is expected as the embankments of the reservoir should be easily detected as their measurements should be of high amplitude. Point 3 and 4 also have concentration of P_T of at least 75%. All other target points have P_T ranging between 1% and 99%. However, their median P_T is at least 80%. The fluctuations with P_T could be due to the reason that these target points are buoys of a rather small size. These buoys are of a diameter less than 0.5m. Their size and the motion due to wind and current can result in measurements with lower amplitude when they are partially ensonified by the sonar.

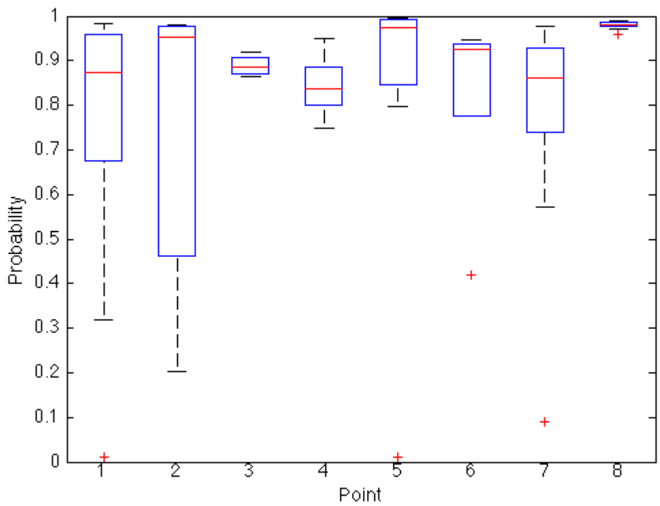

FIGURE 5.11: P_T of the target points at Pandan Reservoir

Target	P_T		
	Min	Median	Max
Point 1	0.0100	0.6245	0.8801
Point 2	0.0969	0.7791	0.8651
Point 3	0.6079	0.6406	0.7055
Point 4	0.4660	0.5688	0.7670
Point 5	0.0100	0.8393	0.9540
Point 6	0.2113	0.7191	0.7597
Point 7	0.0449	0.6030	0.8532
Point 8	0.7927	0.8702	0.9089

TABLE 5.2: P_T statistics of the target points at Pandan Reservoir

5.4.4 Occupancy Grid

The result of the occupancy grid is in Fig. 5.12. All the target points are detected. However, there are artifacts observed at the extreme end of the sonar ensonification. This is because measurements that are farther away are more susceptible to noise and this results in higher false alarm. We analyze the measurements of the objects against their respective $\tilde{S}$, P_T and P_O from Fig. 5.13 to Fig. 5.16.

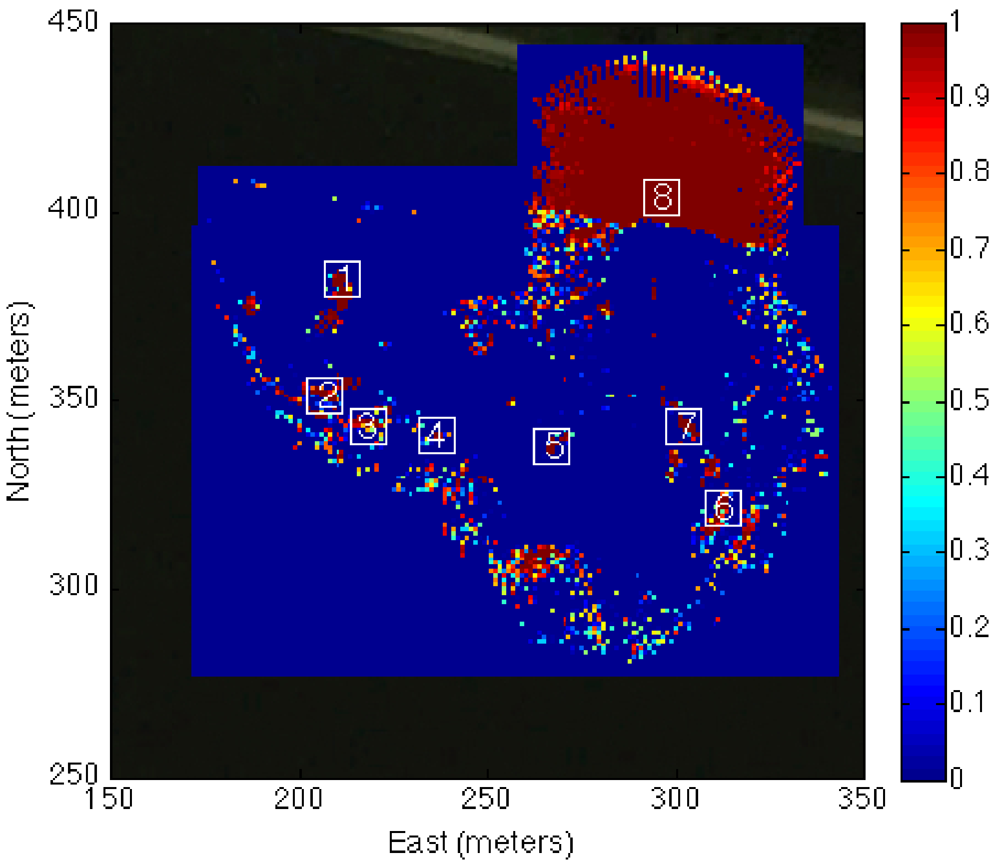

FIGURE 5.12: Result of occupancy grid with static thresholding for Pandan Reservoir dataset

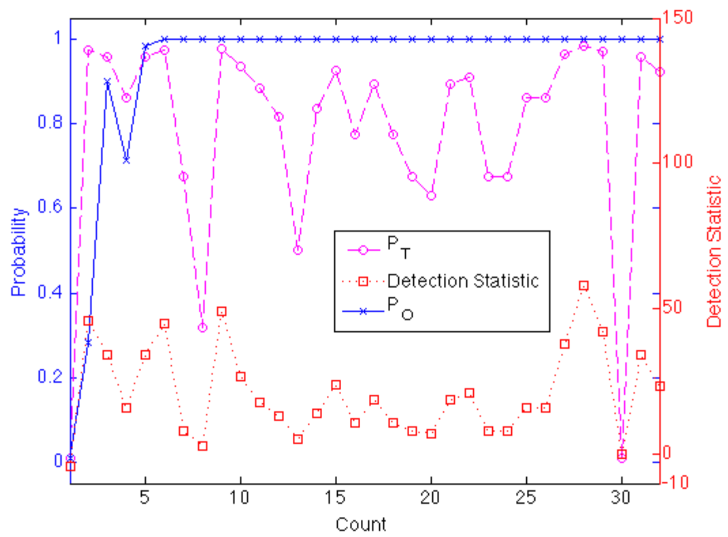

FIGURE 5.13: Plot of P_T, $\tilde{S}$ and P_O of Point 1 at Pandan Reservoir

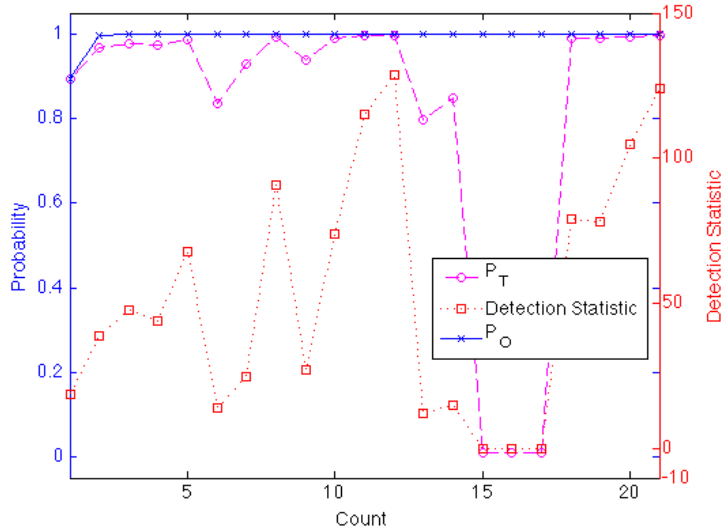

FIGURE 5.14: Plot of P_T, $\tilde{S}$ and P_O of Point 5 at Pandan Reservoir

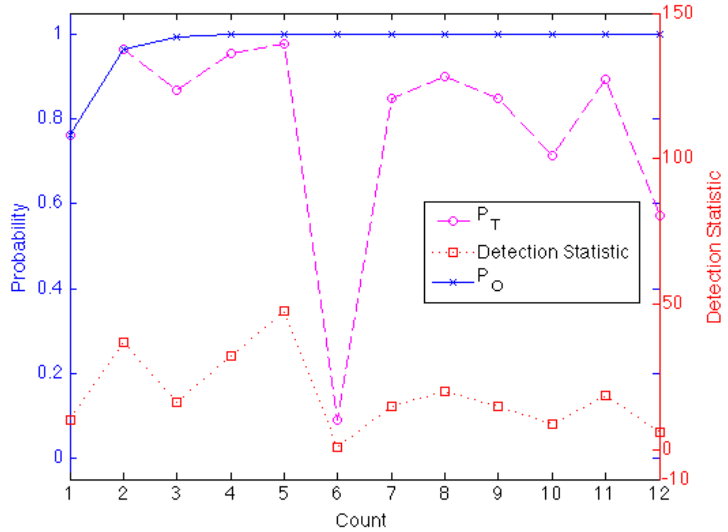

FIGURE 5.15: Plot of P_T, $\tilde{S}$ and P_O of Point 7 at Pandan Reservoir

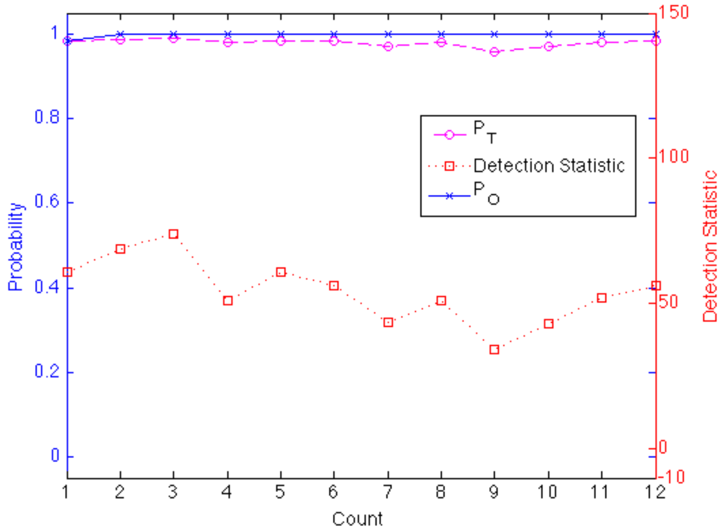

FIGURE 5.16: Plot of P_T, $\tilde{S}$ and P_O of Point 8 at Pandan Reservoir

The observations made on $\tilde{S}$, P_T and P_O are as follows:

Point 1	Its $\tilde{S}$ fluctuate between 0 and 50. The initial $\tilde{S}$ resulted in high P_T and P_O. However, its $\tilde{S}$ decreases and this also resulted in the decrease of P_T and P_O. At the 4th measurement till the 6th measurement, its $\tilde{S}$ increases gradually. Then, its P_O also increases and remain high throughout even when there were subsequently decision statistic that were of lower value.
Point 2, 5, 6, 7	The initial few $\tilde{S}$ result in high P_T with a high value of P_O throughout. Subsequently, its $\tilde{S}$ decreases but that did not reduce P_O.
Point 3, 4, 8	Its $\tilde{S}$ were of high value throughout. These result in high value of P_T and P_O throughout.

5.5 Summary

The embankments and all the target points are easily detected with both thresholding methods. However, the Otsu thresholding failed to filter out non-objects as the entire image is filled with artifacts. The result using static thresholding is more positive as there were only patches of artifacts observed in the occupancy grid. These artifacts however correspond to the high amplitude measurements observed in the raw measurements. The results and observations using Otsu thresholding and static thresholding can be summarized in Table 5.3.

	Otsu Thresholding	Adaptive Thresholding
Threshold	The median threshold determined over 44 iterations is at the value of 33. There is an increase of the threshold when the AUV was already heading straight towards the embankments that are of high amplitude.	The background estimate is higher than the estimate made for NTU and RSYC.
Detection	Embankments are detected.	
	All target points are identified.	
	The entire image is basically filled with artifacts although all the target points are identified.	There are patches of artifacts observed at the extreme end of the sonar ensonification. However, these artifacts also correspond to the high amplitude measurements observed in the raw measurements.
Others	Several scanline measurements have to be collated to form a sectorial image. In a dynamic setup, it is easy to collate the scanline measurements when the AUV is travelling in a straight path. When the AUV is making a turn at high speed, it is not easy collating adjacent and continuous scanline measurements.	Background sector was easy to identify as it was identified during the initialization of the mission.

Table 5.3: Summary of detection methods for Pandan dataset

Chapter 6

Experimental Data — Dynamic Setup by University of Girona

6.1 Experimental Setup

An experiment with the Tritech Miniking sonar was conducted by University of Girona [17] at the Fluvia Nautic abandoned marina near St Pere Pescador (Spain) in 16 March 2007. This experiment involves a dynamically moving AUV scanning the embankments of the marina. The AUV was equipped with a Tritech Miniking sector scanning sonar which is similar to the Micron DST. In this experiment, the sector scanning sonar was configured for a 50m range with 500 bins. A satellite view along with the sonar rendering of the marina can be seen in Fig. 6.1 and Fig. 6.2. In Fig. 6.2, there are artifacts observed at the extreme end of the sonar ensonification. This is because measurements that are farther away are more susceptible to noise and this results in higher false alarm. A similar observation was also made for the dataset at Pandan Reservoir in Chapter 5.

Figure 6.1: Satellite view of the Fluvia Nautic marina

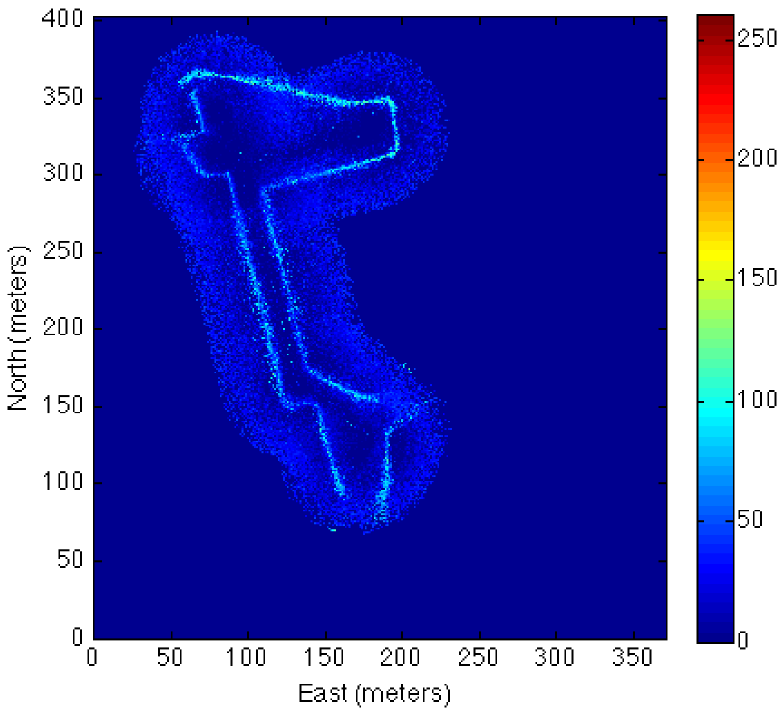

FIGURE 6.2: Sonar rendering of the Fluvia Nautic marina

6.2 Measurement Statistics

We analyze the measurement statistics of the detected embankment at the marina. Fig. 6.3 depicts several of the target points identified to represent the sides of the embankment. The AUV was in motion throughout the mission and the ensonification of the target points could occur from varying distances and bearings. The measurements of the target points are categorized according to their respective object as in Fig. 6.4. If we were to plot the measurements against bin, the representation is inaccurate because measurements at different bins have differing annular statistics, propagation loss and processing gain. The statistic of the measurements are also summarized in Table 6.1.

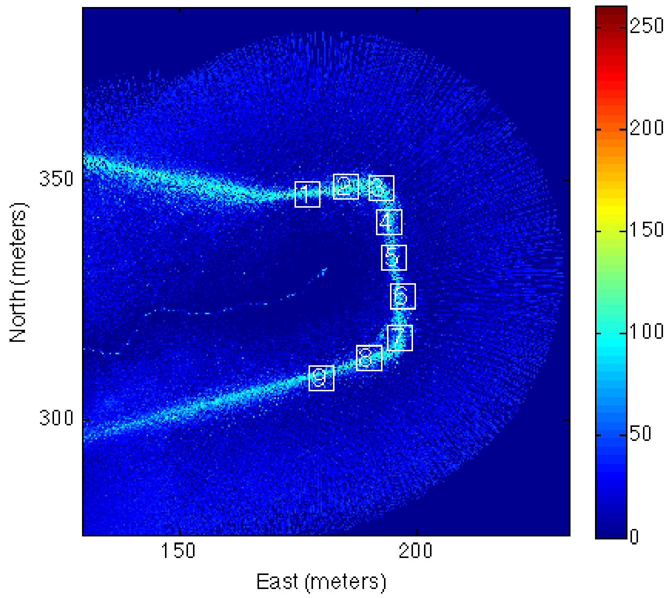

FIGURE 6.3: Target points identified for Girona dataset

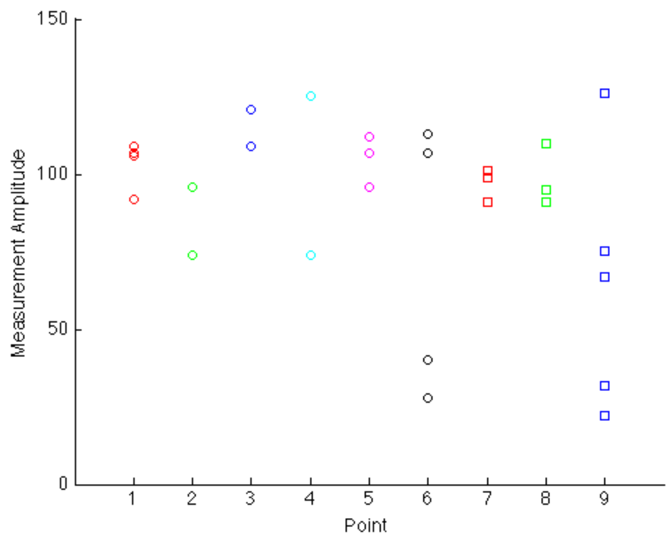

FIGURE 6.4: Measurements of the target points identified for Girona dataset

Measurement	Point								
	1	2	3	4	5	6	7	8	9
Min	92	74	109	74	96	28	91	91	22
Median	106.5	85	115	99.5	107	73.5	99	95	67
Max	109	96	109	125	112	113	101	110	126

TABLE 6.1: Measurement statistics of the target points identified for Girona dataset

6.3 Otsu Thresholding

The Otsu threshold in (2.8) is computed based on the statistics of several scanline measurements that were collated to form a sectorial image. We collated 100 scanline measurements with a field of view of 180°. There were 323 iterations and the thresholds determined are presented in Fig. 6.5. The threshold ranges from 22 to 53 with a median value of 31. The threshold is slightly lower between the 50th till the 150th iterations. This is because the AUV was heading into the large area without any objects in the middle of the marina located at the upper left region of Fig. 6.2. The measurements attained are of lower value as there are less ensonifications of the embankments. At other times, there were more ensonifications of the embankments that result in more measurements with high value.

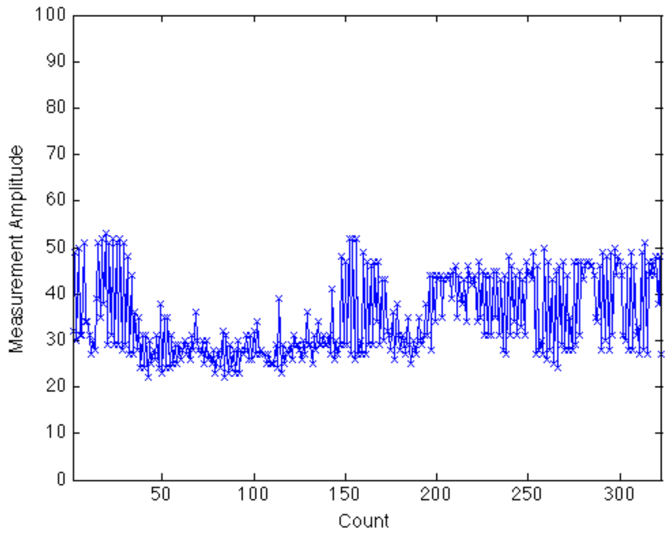

FIGURE 6.5: Otsu threshold for Girona dataset

6.3.1 Binary Occupancy Grid

The result of the median grid cells is in Fig. 6.6. The embankments are easily detected. There are a lot of artifacts detected in the upper region of the marina that are also observed in Fig. 6.2. Based on satellite view of the marina as in Fig. 6.1, we cannot ascertain whether there are objects at that location. Nonetheless, as these measurements exceed the Otsu threshold, these artifacts are considered as objects. There are also artifacts observed at the extreme end of the sonar ensonification. This is similar to the observation in Fig. 6.2.

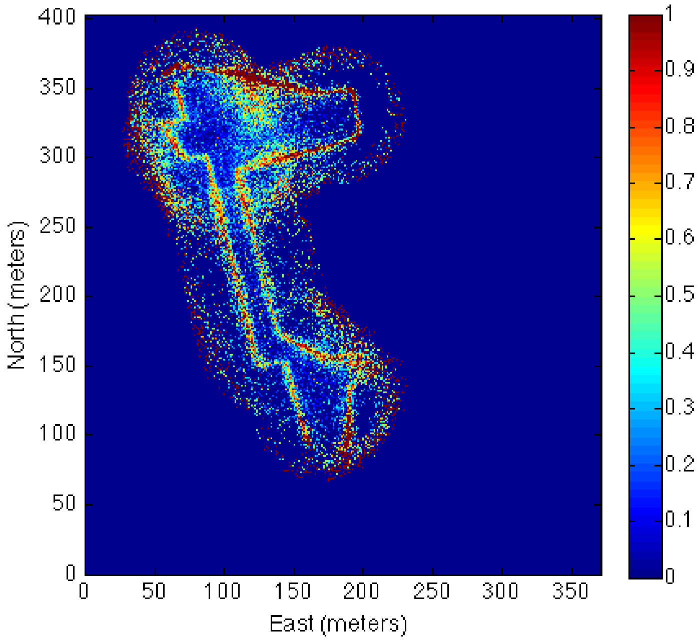

FIGURE 6.6: Mean result of the binary occupancy grid with Otsu thresholding for Girona dataset

In Fig. 6.7 to Fig. 6.9, we analyze the measurements of the objects against their respective Otsu threshold to understand the results of binary detection.

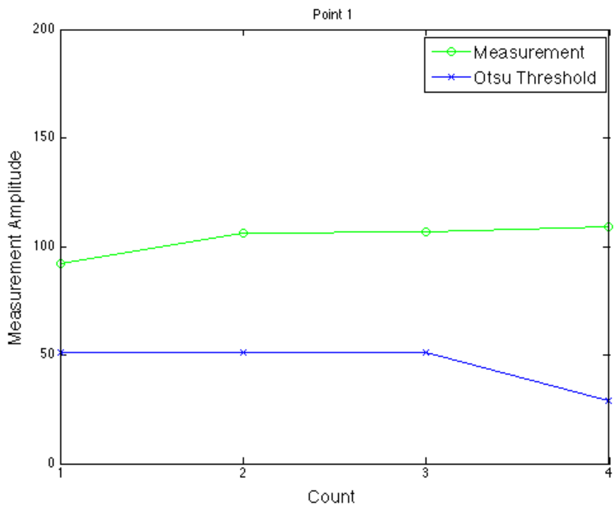

FIGURE 6.7: Binary detection of Point 1 for Girona dataset

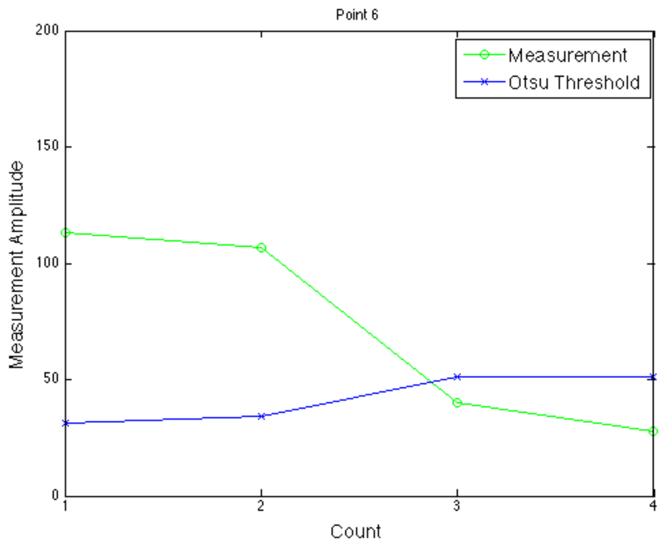

FIGURE 6.8: Binary detection of Point 6 for Girona dataset

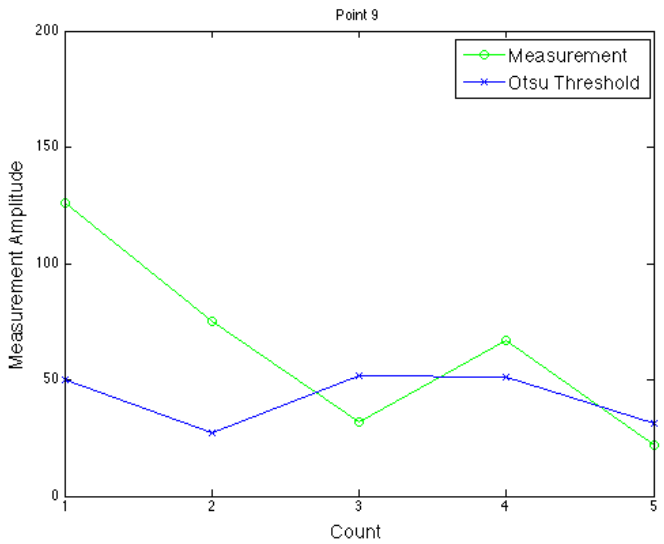

FIGURE 6.9: Binary detection of Point 9 for Girona dataset

The statistics of the binary detections are summarized in Table 6.2. All the measurements for the target points exceed the Otsu threshold except for Point 6 and 9 that have several measurements below the threshold. However, all the target points can be identified with mean statistics.

Point	No. of Positive Detection	No. of Measurements	Percentage (%)
1	4	4	100
2	2	2	100
3	2	2	100
4	2	2	100
5	3	3	100
6	2	4	50
7	3	3	100
8	3	3	100
9	3	5	60

TABLE 6.2: Statistics of binary detection for the target points identified for Girona dataset

6.4 Static Thresholding

6.4.1 Background Statistics

Firstly, we analyze the statistics of the background noise that are free of targets. We identify a sector located at the top right area within the orange-colored boundary in Fig. 6.10 that are free of objects as a suitable sample dataset for background statistics processing. The background statistics gradually increases from around bin 100 to bin 400 before it becomes rather constant subsequently. There are several spurious spikes observed. These spikes could be due to to the water surface's wakes that results in the measurements having higher amplitude.

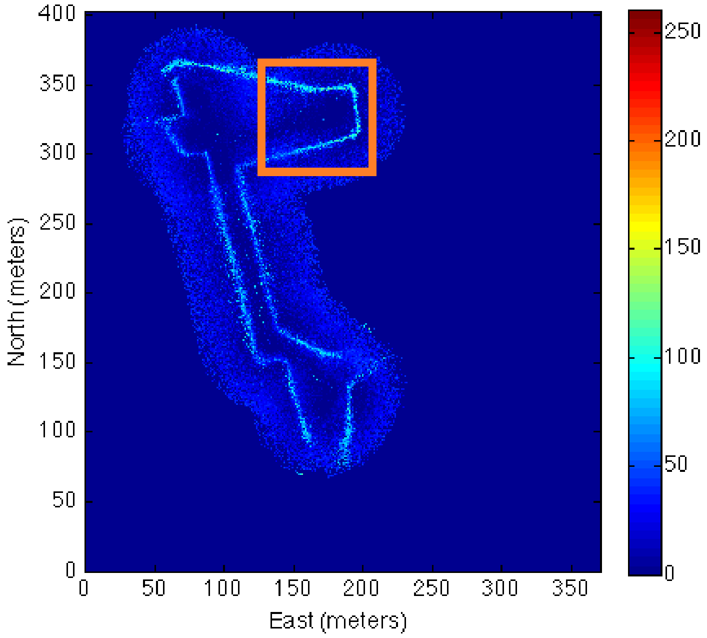

FIGURE 6.10: Background sector identified within the orange-colored boundary for Girona dataset

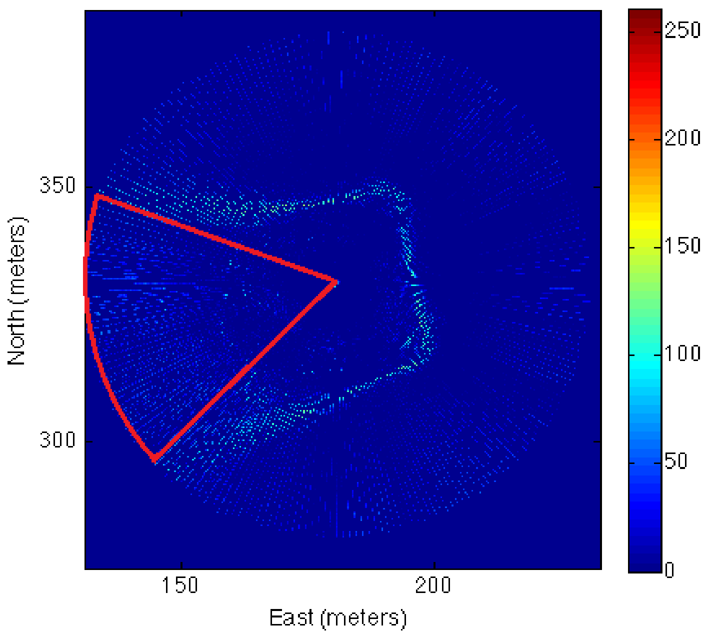

FIGURE 6.11: Zoom in on the background sector identified for Girona dataset

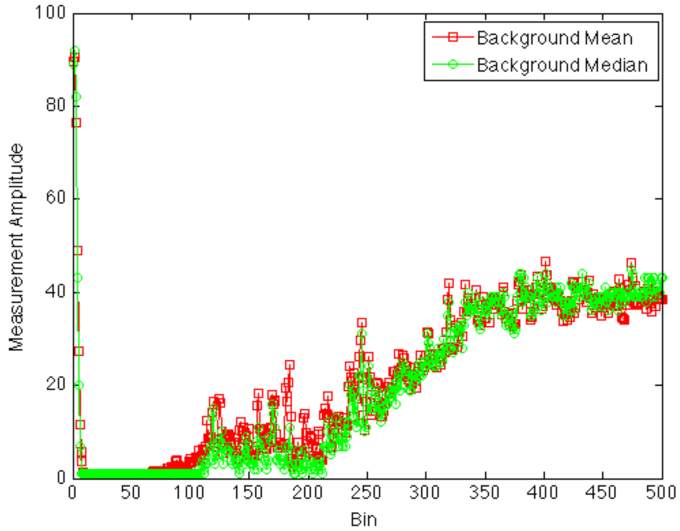

FIGURE 6.12: Statistics of the background sector identified for Girona dataset

Subsequently, assuming the P_{FA} is set for 1% with the number of background statistics, N_i, as 41, the threshold constant K in (2.10) can be determined as:

$$\begin{aligned} K &= \sqrt{\left[(P_{FA})^{-\frac{1}{N_i}} - 1\right] N_i} \\ &= \sqrt{\left[(0.01)^{-\frac{1}{41}} - 1\right] 41} \\ &= 2.2077 \end{aligned} \tag{6.1}$$

6.4.2 Decision Statistic

The decision statistic $\tilde{S}$ of the target points for Girona dataset is estimated as in (2.1). The computed $\tilde{S}$ of the objects are depicted in Fig. 6.13.

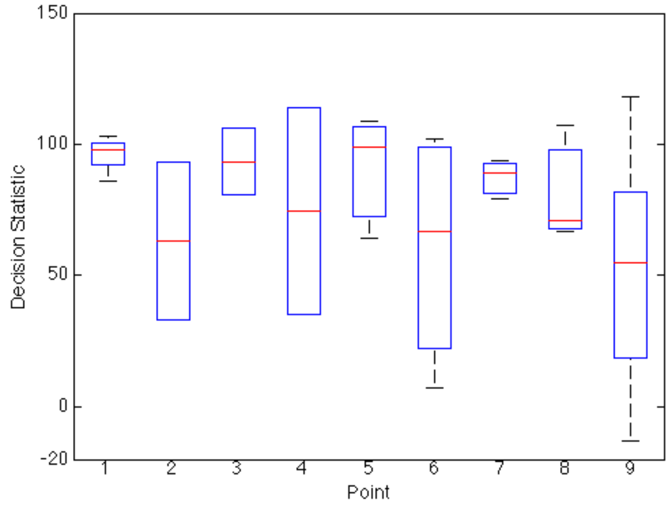

FIGURE 6.13: Decision statistic of the target points identified for Girona dataset

Point 1, 3, 5, 7 and 8 have decision statistic of at least 60. These targets are expected to easily have high P_T. Point 2 and 4 have median decision statistic of at least 60 but their minimum decision statistic is around 30. These targets might also have high P_T. Point 6 and 9 have the most extreme fluctuations. The decision statistic for Point 6 ranges from 6 to around 100 while Point 9 ranges from negative decision statistic to around 100. However, Point 6 and 9 also have median statistic of around 60. Point 6 and 9 might also have high P_T.

6.4.3 Probability of Target

Assuming P_{FA} is set for 1% with the number of background statistics, N_i, as 8, P_T in (2.12) is computed as in Fig. 6.14.

$\tilde{S}$	Point								
	1	2	3	4	5	6	7	8	9
Min	86	33	81	35	64	7	79	67	-13
Median	98	63	93.5	74.5	99	67	89	71	55
Max	103	93	106	114	109	102	94	107	118

TABLE 6.3: Decision statistic of the target points identified for Girona dataset

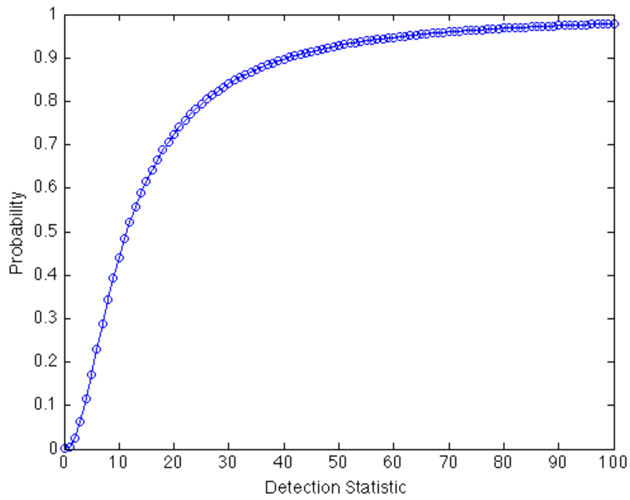

FIGURE 6.14: P_T for Girona dataset

Based on the decision statistic of the targets as in Fig. 6.13, the P_T for all the targets can be summarized as in Fig. 6.15 and Table 6.4. The observations made earlier in Section 6.4.2 about the P_T for the all target points are as expected. Point 6 and 9 respectively have minimum P_T of 62% and 1%. However, all the target points have median P_T of at least 97%. These implies that all the target points are easily detected.

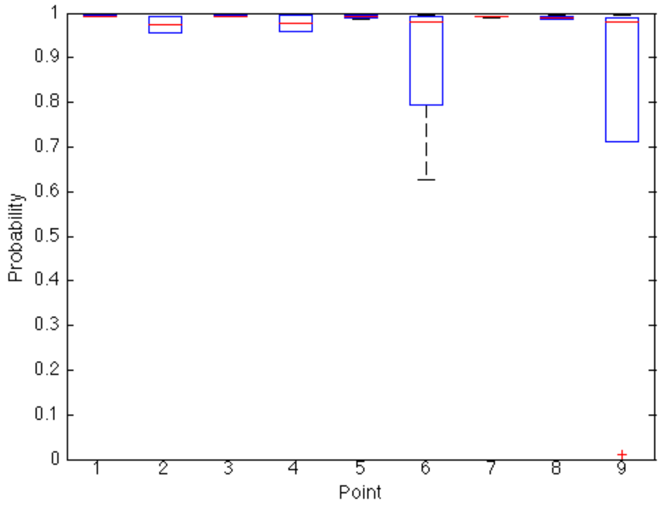

FIGURE 6.15: P_T of the target points identified for Girona dataset

Point	P_T		
	Min	Median	Max
1	0.9919	0.9937	0.9943
2	0.9552	0.9741	0.9930
3	0.9910	0.9928	0.9946
4	0.9595	0.9774	0.9953
5	0.9861	0.9938	0.9948
6	0.6251	0.9791	0.9942
7	0.9906	0.9924	0.9932
8	0.9872	0.9885	0.9947
9	0.01	0.9817	0.9956

TABLE 6.4: P_T of target points identified for Girona dataset

6.4.4 Occupancy Grid

The result of the occupancy grid is in Fig. 6.16. All the target points and embankments are detected. There are also less artifacts observed within the marina and beyond the embankments. The artifacts that were observed in the upper region of the marina in the median statistics were not observed based on the static thresholding methodology. We analyze the measurements of the objects against their respective $\tilde{S}$, P_T and P_O from Fig. 6.17 to Fig. 6.20.

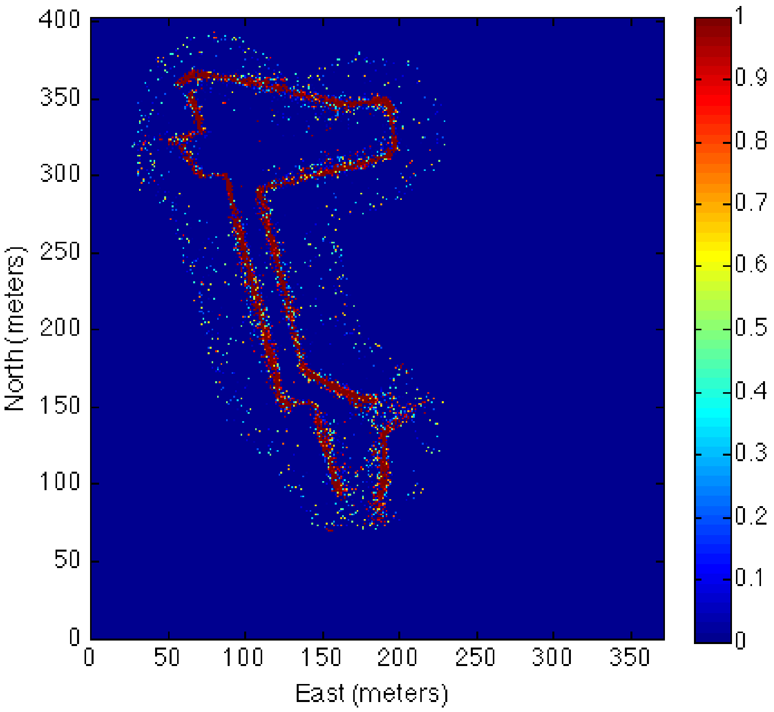

FIGURE 6.16: Result of occupancy grid with static thresholding for Girona dataset

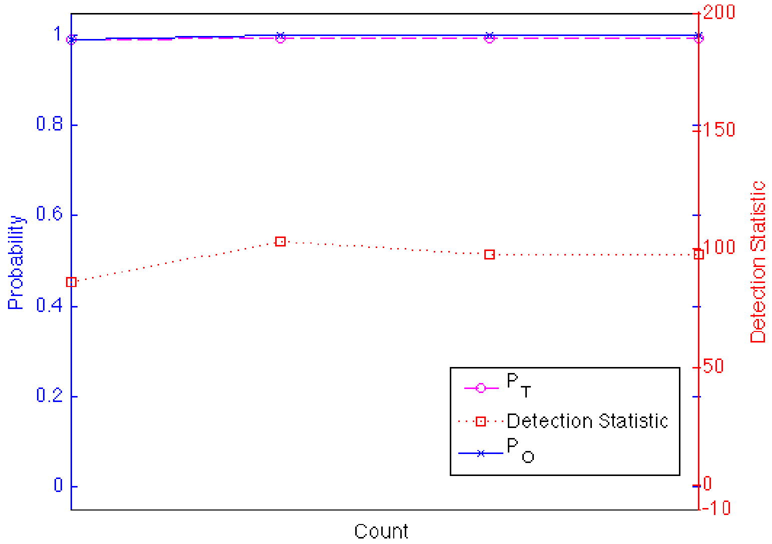

FIGURE 6.17: Plot of P_T, $\tilde{S}$ and P_O of Point 1 for Girona dataset

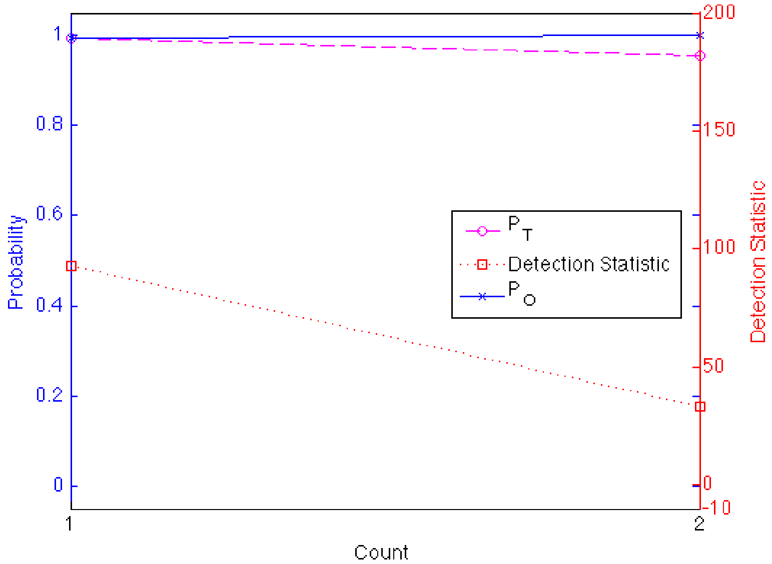

FIGURE 6.18: Plot of P_T, $\tilde{S}$ and P_O of Point 2 for Girona dataset

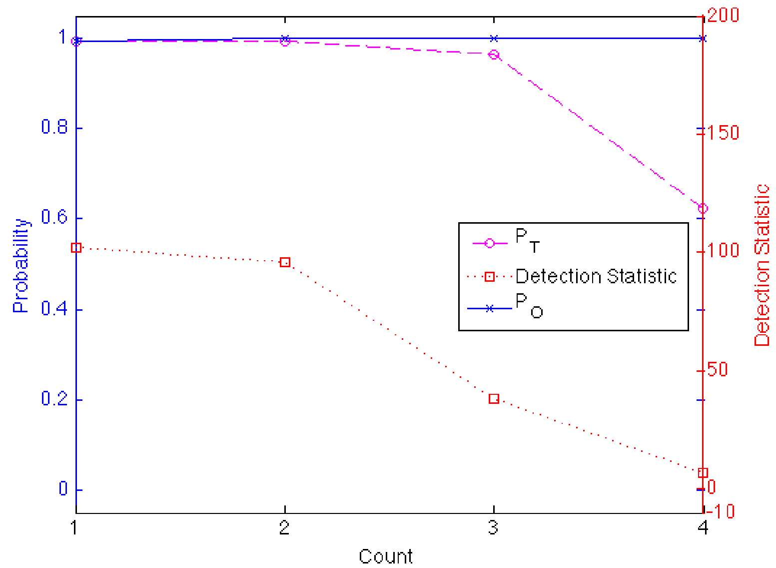

FIGURE 6.19: Plot of P_T, $\tilde{S}$ and P_O of Point 6 for Girona dataset

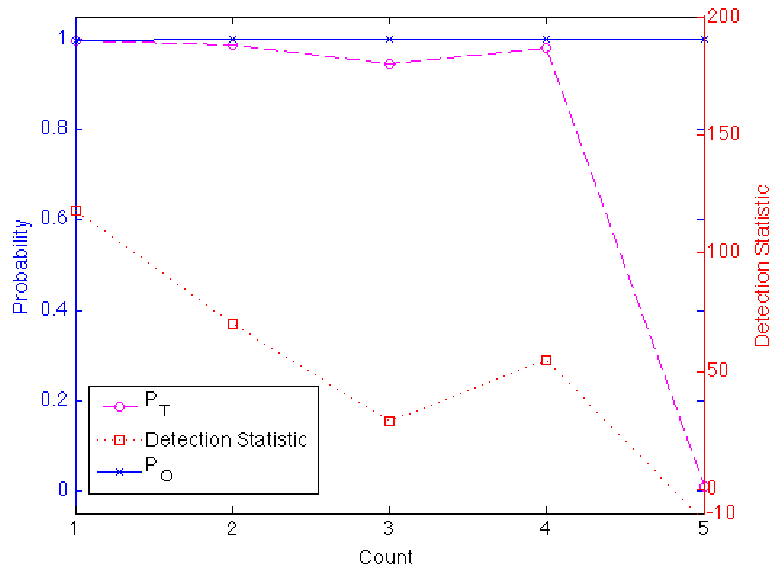

FIGURE 6.20: Plot of P_T, $\tilde{S}$ and P_O of Point 9 for Girona dataset

The observations made on $\tilde{S}$, P_T and P_O are presented as follows:

Point 1 — All the measurements resulted in P_T of at least 95% because the detection statistic was

	nearing 100 throughout. P_0 was easily high throughout.
Point 2, 3, 4, 5, 7, 8	Their $\tilde{S}$ decreased and this resulted in a slightly decreasing P_T. However, P_0 was already high due to the initial $\tilde{S}$ that was high. P_0 remained high throughout.
Point 6	Its $\tilde{S}$ decreased and this resulted in decreasing P_T that was more steep as compared to the observations for Point 2, 3, 4, 5, 7 and 8. The decrease of P_T was steep because $\tilde{S}$ was nearing 0. However, P_0 was already high due to the initial $\tilde{S}$ that was high. P_0 remained high throughout.
Point 9	Its $\tilde{S}$ was decreasing throughout except at the 4th measurement where it did increased once. P_T follows the trend of $\tilde{S}$ but was less steep and responsive. However, the last $\tilde{S}$ was negative. This caused P_T to drop from near 95% to almost 0%. However, P_0 remained high throughout because the initial few measurements already resulted in high P_0.

6.5 Summary

The embankments and all the target points are easily detected with both thresholding methods. The result based on Otsu thresholding yields a lot of artifacts as compared to the result using static thresholding. The detection of the embankments based on static thresholding was more effective than Otsu thresholding. The results and observations using Otsu thresholding and static thresholding can be summarized in Table 6.5.

<table>
<tr><th></th><th>Otsu Thresholding</th><th>Adaptive Thresholding</th></tr>
<tr><td>Threshold</td><td>The threshold ranges from 22 to 53 with a median value of 31 over 323 iterations.The threshold is slightly lower when the AUV was heading into the large empty area</td><td>The background estimate gradually increases with several spikes observed throughout.</td></tr>
<tr><td rowspan="4">Detection</td><td colspan="2">Embankments are detected.</td></tr>
<tr><td colspan="2">All target points are identified.</td></tr>
<tr><td>There are a lot of artifacts detected.</td><td>There are also less artifacts observed within the marina and beyond the embankments.</td></tr>
<tr><td>The binary detection of the embankments were not all at 100%. There were binary detections of 0%. However, median detection was still at 50%.</td><td>The detection of the embankments were mostly at 90%.</td></tr>
<tr><td>Others</td><td>Several scanline measurements have to be collated to form a sectorial image. In a dynamic setup when the AUV is travelling at a slow speed, it is easy to collate the scanline measurements.</td><td>Background sector was easy to identify as it was identified during the initialization of the mission. However, the difficulty was in ensuring whether the background sector is indeed free of any objects.</td></tr>
</table>

TABLE 6.5: Summary of detection methods for Girona dataset

Chapter 7

Conclusion and Future Work

7.1 Conclusion

Detection methodologies with Otsu thresholding and static thresholding were analyzed on four experimental datasets spanning from statically deployed sector scanning sonar to a dynamic setup involving a moving AUV. In addition, the concept of occupancy grid also was analyzed as a means for a representation methodology. Although Otsu thresholding [3] was able to detect the background and foreground modes to obtain the threshold to discriminate them, a lot of artifacts were observed. It lacks the ability to discount measurements that were marginally higher than the threshold as non-objects. The Otsu thresholding was effective for the NTU, RSYC and

Girona datasets but it failed drastically for the dynamic setup using the AUV at Pandan Reservoir.

The static thresholding was effective in detecting objects across the four experimental datasets. In addition, there were significantly less artifacts observed. The assignment of P_T which is the probability of a target given a measurement was considered based on the $\tilde{S}$ which is the detection statistic of the measurement. The higher the $\tilde{S}$, the higher the probability P_T was accorded. It was then effectively able to progressively discount measurements that were marginally higher than the threshold as non-objects. Occupancy grid also proved to be an effective representation of the environment. We adopt P_T into the formulation of occupancy grid to attain probabilistic statement of object detection. Each grid cell can be independently updated as and when more measurements are attained.

7.2 Future Work

Firstly, one of the observations made consistently across the NTU, RSYC, Pandan and Girona datasets was that it was difficult to identify a sector to estimate the background's noise statistics. We can attempt to determine a sector with an assumption that there are no objects but this is only to the best of our knowledge and understanding of the operating environment. We can also attempt to ensure that there are no objects in the sector during calibration. However, this approach is not cost and time effective when there are a lot of unknown environments where the AUV can be deployed. An efficient and accurate estimation of the background statistics allows for a more refined probability of detection. Future efforts here would entail investigating into various methods of noise level estimation and potentially a real-time calibration algorithm.

Secondly, the NTU and RSYC datasets are with a static sector-scanning sonar. The Girona dataset [17] was with a slow-moving underwater vehicle while the Pandan dataset was conducted with the STARFISH AUV in a confined water environment. The next step would be to analyze datasets from an operational STARFISH AUV [1, 2] in open waters and various other confined water environments. In addition, analysis would be extended to moving targets. Future efforts would entail developing software(s) capable of real-time processing of the sonar data along with real-time object(s) detection within the processing unit of the AUV.

Thirdly, in a real-world scenario, the operating environment can vary from one extreme to another. The expected probability of objects in an open water environment can be very low while a high probability can be expected when operating in a marina. Prior information pertaining to the operating environment can be advantageously used as an initialization parameter (2.15) for the occupancy grid [Section 2.3].

Bibliography

[1] T. B. Koay, Y. T. Tan, Y. H. Eng, R. Gao, M. Chitre, J. L. Chew, N. Chandhavarkar, R. Khan, T. Taher, and J. Koh, “Starfish - a small team of autonomous robotics fish,” *Indian Journal of geo-Marine Science*, vol. 40, pp. 157–167, April 2011.

[2] J. L. Chew, T. B. Koay, Y. T. Tan, Y. H. Eng, R. Gao, M. Chitre, and N. Chandhavarkar, “Starfish: An open-architecture auv and its applications,” in *Defense Technology Asia 2011*, Feb 2011.

[3] N. Otsu, “A threshold selection method from gray-level histograms,” *Systems, Man and Cybernetics, IEEE Transactions on*, vol. 9, no. 1, pp. 62–66, 1979.

[4] H. K. Heidarsson and G. S. Sukhatme, “Obstacle detection and avoidance for an autonomous surface vehicle using a profiling sonar,” in *Robotics and Automation (ICRA), 2011 IEEE International Conference on*, May 2011, pp. 731 –736.

[5] L. Henriksen, “Real-time underwater object detection based on an electrically scanned high-resolution sonar,” in *Autonomous Underwater Vehicle Technology, 1994. AUV '94., Proceedings of the 1994 Symposium on*, July 1994, pp. 99 –104.

[6] H. Finn and R. Johnson, “Adaptive detection mode with threshold control as a function of spatially sampled clutter-level estimates,” *RCA Review*, vol. 29, no. 3, pp. 414 – 464, 1968.

[7] P. Mclane, P. Wittke, and C.-S. Ip, “Threshold control for automatic detection in radar systems,” *Aerospace and Electronic Systems, IEEE Transactions on*, vol. AES-18, no. 2, pp. 242 –248, March 1982.

[8] P. P. Gandhi and S. A. Kassam, “Analysis of cfar processors in non-homogeneous background,” *Aerospace and Electronic Systems, IEEE Transactions on*, vol. 24, no. 4, pp. 443–454, 1988.

[9] M. Smith and P. Varshney, “Intelligent cfar processor based on data variability,” *Aerospace and Electronic Systems, IEEE Transactions on*, vol. 36, no. 3, pp. 837 –847, July 2000.

[10] B. Kalyan and A. Balasuriya, “Sonar based automatic target detection scheme for underwater environments using cfar techniques: a comparative study,” in *Underwater Technology, 2004. UT ’04. 2004 International Symposium on*, 2004, pp. 33–37.

[11] M. A. Richards, *Fundamentals of Radar Signal Procesing.* McGraw-Hill, 2005.

[12] S. Zhao, T.-F. Lu, and A. Anvar, “Automatic object detection for auv navigation using imaging sonar within confined environments,” in *Industrial Electronics and Applications, 2009. ICIEA 2009. 4th IEEE Conference on*, May 2009, pp. 3648 –3653.

[13] S. Zhao, T.-F. Lu, and A. Anvar, “Multiple obstacles detection using fuzzy interface system for auv navigation in natural water,” in *Industrial Electronics and Applications (ICIEA), 2010 the 5th IEEE Conference on*, 2010, pp. 50 –55.

[14] I. Quidu, A. Hetet, Y. Dupas, and S. Lefevre, “Auv (redermor) obstacle detection and avoidance experimental evaluation,” in *OCEANS 2007 - Europe*, June 2007, pp. 1–6.

[15] A. Elfes, “Using occupancy grids for mobile robot perception and navigation,” *Computer*, vol. 22, no. 6, pp. 46 –57, June 1989.

[16] Tritech. (2013, July) Micron dst sector scanning sonar. [Online]. Available: http://www.tritech.co.uk/product/small-rov-mechanical-sector-scanning-sonar-tritech-micron

[17] D. Ribas, P. Ridao, J. Tardós, and J. Neira, "Underwater SLAM in man made structured environments," *Journal of Field Robotics*, vol. 25, no. 11-12, pp. 898–921, November - December 2008.

[18] P. Swerling, "Probability of detection for fluctuating targets," *Information Theory, IRE Transactions on*, vol. 6, no. 2, pp. 269–308, 1960.

[19] S. Thrun, W. Burgard, and D. Fox, *Probabilistic Robotics.* The MIT Press, 2005.